Micro and Nanostructures for Two-phase Fluid and Thermal Transport

by

Yangying Zhu

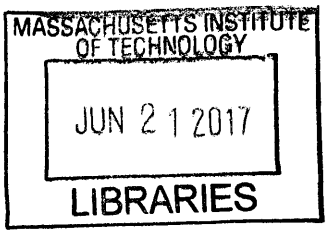

ARCHIVES

Submitted to the Department of Mechanical Engineering in partial fulfillment of the requirements for the degree of

Doctor of Philosophy

at the

MASSACHUSETTS INSTITUTE OF TECHNOLOGY

June 2017

Author..... Signature redacted .....
Department of Mechanical Engineering
May 25, 2017

Certified by..... Signature redacted ...
Evelyn N. Wang
Gail E. Kendall Associate Professor
Thesis Supervisor

Accepted by..... Signature redacted .....
Rohan Abeyaratne
Chairman, Department Committee on Graduate Students

Micro and Nanostructures for Two-phase Fluid and Thermal Transport

by

Yangying Zhu

Submitted to the Department of Mechanical Engineering
on May 25, 2017, in partial fulfillment of the
requirements for the degree of
Doctor of Philosophy

Abstract

This thesis aims to develop fundamental understanding of the role of surface structures in two-phase heat sinks including capillary driven evaporators and flow boiling in microchannels. First, we developed a detailed finite volume numerical model for thin-film evaporation from micropillar array wick structures. The model can predict the dry-out heat flux on various micropillar structure geometries (diameter, pitch, and height) in the length scale range of 1–100 μm and capture the optimal geometries to maximize the dry-out heat flux. The model suggests that maximizing the capillary flow requires a high capillary pressure gradient and a low viscous flow resistance, and that only considering one factor can lead to a low dry-out heat flux. Guided by the model, we then designed and fabricated microchannel heat sink devices incorporated with surface structures. Specifically, we decouple nucleation and thin film evaporation through the design of two different surfaces on the sidewall and the heated bottom surface. Bubbles can be generated at the less hydrophilic sidewalls while the superhydrophilic microstructures on the heated surface of the channel can maintain a liquid film by capillary wicking to promote thin film evaporation and prevent dry-out. Our experimental results show significantly reduced long-timescale (~seconds) temperature and pressure drop fluctuation at high heat fluxes. A critical heat flux (CHF) of 969 W/cm^2 was achieved with a structured surface, a 57% enhancement compared to a smooth surface. The trend of CHF enhancement among different geometries of the structures agrees well with the fluid wicking model, which suggests that capillarity is the key factor contributing to the enhanced performance. Furthermore, we investigated the temperature response as a result of short-timescale (~ms) flow oscillation. The surface structures also significantly suppress the magnitude of this high-frequency temperature oscillation and potentially can improve the reliability of these two-phase heat sinks with reduced mechanical and thermal fatigue. The insights gained from these works lead to new design principles for advanced thermal management solutions for high power density electronic systems in the future.

Thesis Supervisor: Evelyn N. Wang

Title: Gail E. Kendall Associate Professor

Acknowledgement

This thesis would not have been possible without the guidance, support and inspiration from my mentors, colleagues, friends and family. First and foremost, I would like to sincerely thank my thesis advisor, Professor Evelyn Wang. She introduced me into the exciting world of micro and nanotechnology and guided me through obstacles and challenges in research. She has a deep vision and high standards but she is also patient and gives me the freedom to explore topics of my interest. She is extremely enthusiastic about research, teaching and mentoring, and as a female professor, has inspired me in many ways to continue pursuing engineering and science in my future career.

I would also like to thank my thesis committee, Prof. Gang Chen and Prof. John Lienhard, who provided me insightful advice and asked critical questions that helped improve the quality of this thesis. I also feel extremely lucky to work in the Rohsenow Kendall Heat Transfer Lab, shared among my thesis committee members, that allows me to interact with and learn from many of their students and postdocs working in the similar area. I want to also thank Prof. TieJun Zhang at Masdar Institute of Science and Technology for many helpful discussions throughout my graduate study.

Many former and current labmates at the Device Research Laboratory have provided me tremendous help and encouragement. I would like to thank Dr. Rong Xiao, Dr. Kuan-Han Chu, Dr. Ryan Enright and Dr. Youngsuk Nam for their guidance on my master's research when I just started my graduate study at MIT, Dr. Rishi Ray and especially Dr. Dion Antao for their help with the flow boiling research. I want to thank everyone at DRL for their support, collaboration, friendship, and encouragement. I would like to thank many staff members at the Microsystems Technology Laboratory for their support, especially Dennis Ward who spent an incredible number of hours helping me with using the facilities and discussion. I also want to thank my piano teachers at MIT, David Deveau and Marilyn Roth, who have encouraged and inspired me to continue pursuing classical music study. I appreciate funding support from AFOSR, Masdar Institute of Science and Technology, SMART, and ONR.

Last but not the least, I would like to thank my parents for their unconditional love and understanding, without which any of my achievements would have been impossible. I would like to thank my husband Bolin Liao for his unwavering support.

Table of Contents

List of Figures

List of Tables

Chapter 1

Introduction

1.1 Thermal Management Challenges of Electronics

The increasing power densities in modern electronic devices and systems pose significant thermal management challenges. For example, as central processing units (CPUs) have approached heat fluxes of 100 W/cm^2 (Figure 1-1), typical commercial fin-fan based thermal management strategies are no longer able to dissipate the required fluxes while maintaining the chip temperature below their maximum allowable temperature of approximately 85 °C. This has led to the design of multi-core processors.[1] In addition, the thermal management demands for other energy and electronic systems such as concentrated solar photovoltaics (CSP), gallium nitride (GaN) power electronics, and laser diodes, are exceeding heat fluxes of 1000 W/cm^2.[2] In some scenarios, dissipating heat from electronics to meet the requirement of their operating temperature can consume a large amount of energy. The International Technology Roadmap for Semiconductors (ITRS) predicts that by 2029, data centers will consume 482 GWh for facility cooling, in

addition to the 560 GWh power for networking, switching, and storage.[3] Clearly, the need for thermal management schemes that are capable of dissipating high heat fluxes, with small increases in temperature, and which consume low energy has been well recognized.

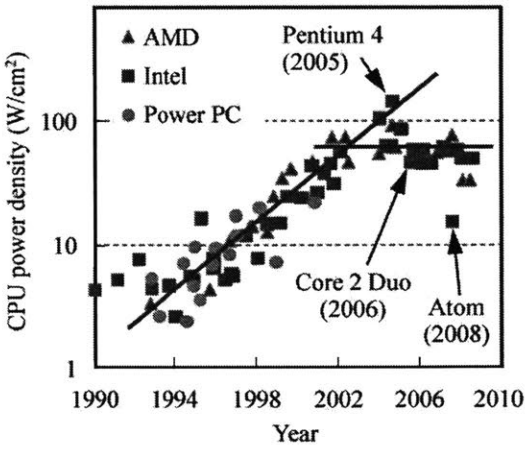

Figure 1-1 Trend of power density of CPUs. Figure from Ref. 1

1.2 Cooling Schemes based on Phase-Change Heat Transfer

Liquid-vapor phase-change heat transfer is a promising approach to address the above mentioned challenges because the latent heat of a fluid is in general 2 – 3 orders of magnitude higher than its specific heat capacity.[4] Boiling, a most common form of liquid-vapor phase-change process, can dissipate orders-of-magnitude higher heat fluxes compared to single-phase air cooling, as shown in Figure 1-2a. The critical heat flux (CHF) is typically defined as the maximum achievable heat flux before severe heat transfer degradation occurs. Thus CHF represents the limitation in heat flux of specific heat transfer modes. Another important metric is the heat transfer coefficient (often denoted as HTC or h), which is typically defined as the ratio between heat flux (q) and the temperature difference (ΔT) between the wall (T_w) and the bulk fluid (T_∞). Heat transfer coefficient represents the thermal conductance for heat to transport from the wall to the bulk fluid. Figure 1-2b shows the comparison of the heat transfer coefficient

among various cooling schemes. Due to the latent heat, the heat transfer coefficient of boiling is usually also higher than single-phase liquid or air convection.

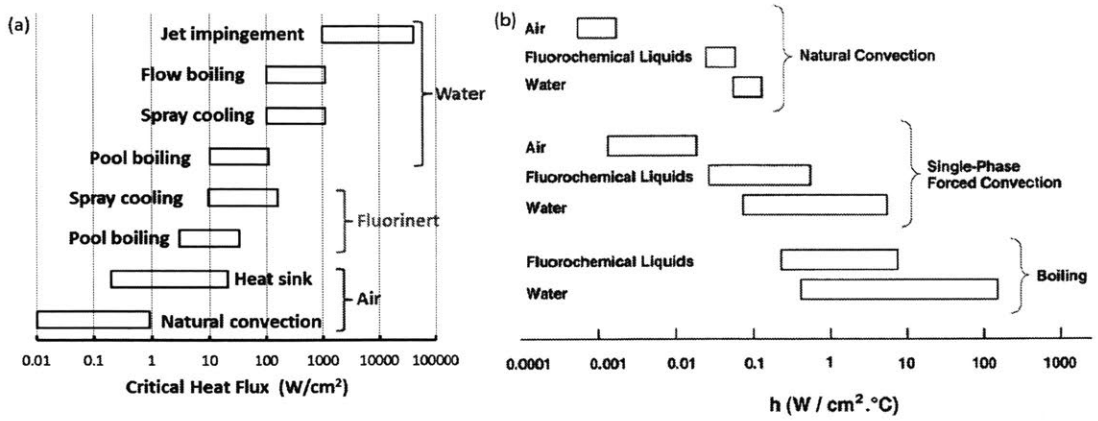

Figure 1-2 (a) Comparison of critical heat flux (CHF), which is the maximum heat flux achievable before severe heat transfer degradation occurs, with air cooling and liquid-vapor phase-change cooling. Data from Ref. 5 and Ref. 6 (b) Comparison of the heat transfer coefficient among various cooling schemes. Adapted from Ref. 7

Both spray cooling[8] and jet impingement[9,10] have the potential to achieve high CHF. In these schemes, liquid from nozzles impinges on the hot surfaces in the form of jet flow or droplets. Typical challenges with these approaches include the requirement of a complex 3D architecture, uneven distribution of the flow and extremely high pressure of the working fluid. Boiling, on the other hand, typically requires simple systems and can operate at pressures close to the atmosphere. In the case of pool boiling, bubbles generated from the hot surface are driven away passively (by buoyancy), which open up space for the subsequent bubbles to nucleate. Thus to continually remove heat, no active pumping is required as opposed to spray cooling and jet impingement. Pool boiling has demonstrated critical heat flux (CHF) values of approximately 100 W/cm^2 with water as the working fluid on smooth surfaces.[11] The cause of CHF on smooth surfaces has commonly been attributed to hydrodynamic instability at the interface of liquid-vapor columns, described by the Zuber model.[11] Besides the fact that CHF values cannot reach the desired high fluxes, pool boiling is typically impractical for implementation with electronic systems because of the large volume required and orientation dependency.

Flow boiling involves liquid-to-vapor phase change occurring in bulk flow in channels. It has the potential to achieve high heat transfer performance because external pumping can aid convective heat transfer as well as help remove the vapor bubbles more

effectively than buoyancy (in pool boiling). In particular, flow boiling in mini and microchannels is attractive for electronics cooling because of its compact form factor and high surface-to-volume ratio that contributes to a low thermal resistance. However, the main challenges with flow boiling are flow instabilities and the need to increase CHF. The main reason for flow instabilities, which typically manifest themselves as mass flow rate fluctuation, is due to the significantly lower density of the vapor phase than the liquid phase. As a result, vapor needs to accelerate substantially to maintain a constant mass flow rate along the channel. This results in a negative slope on the pressure drop vs. mass flow rate curve (internal curve) in the two-phase region with a constant heat flux. The intersection between the internal curve and the external flow characteristics curve can be unstable, which leads to flow rate and pressure drop oscillations. A few types of two-phase flow instabilities are summarized in a review by Kakaç and Bon.[12] When flow instabilities occur, insufficient liquid supply during mass flow rate oscillation can lead to dry-out in the channel, which causes temperature oscillations. As heat flux increases, severe dry-out can develop to critical heat flux condition. Thus, studies on flow boiling in microchannels have focused on various means to mitigate flow instabilities and enhance the CHF.

In addition to flow boiling, evaporation has been commonly used in heat pipes, where heat fluxes in the range of 50 – 100 W/cm^2 have been achieved.[13] In these heat pipe devices, liquid evaporates from a porous media. The evaporated vapor condenses in the condenser and the circulation is passively driven by capillarity generated in the porous media. Although the maximum heat flux currently demonstrated with capillary-driven evaporation schemes is lower compared to flow boiling in microchannels, they are generally simple, stable, and do not require pumping element and power consumption and therefore attractive for some applications. In addition, evaporation and boiling are closely related in that nucleation of a bubble involves evaporation across the bubble interface. Insights gained from evaporation studies often aid the understanding of the more complex boiling phenomena. Similarly, there has been tremendous interest to enhance the heat transfer coefficient and CHF (or dry-out heat flux) for evaporation type of heat transfer schemes. Recent studies suggest that evaporation from thin-film region, where the liquid thickness is on the order of 1 μm, has the highest heat transfer rate.[14]

Increasing the thin-film area while enhancing the capillary flow have the potential to further improve the heat transfer performance.

1.3 Micro and Nanostructures for Liquid-to-Vapor Heat Transfer

Recent advancements in micro and nanotechnology have brought new opportunities to enhance liquid-vapor phase change heat transfer. The ability to engineer surfaces with precise structures and tailored chemistry allows manipulation of wetting and interfaces near the three phase contact line, which plays a key role in the macroscopic heat transfer behavior. Examples include superhydrophobic and superhydrophilic surfaces realized by roughening the surface while either reducing or increasing the surface energy by selective coatings, biphilic surfaces with patterned hydrophilic and hydrophobic regions, surfaces with microcavities, and hierarchical structured surfaces with various length scale features. Many of these surfaces are also inspired by surfaces in nature with various functionalities and morphologies. Some examples include the superhydrophobic lotus leaf which repels water, hydrophilic shells of beetles for water capturing.

Numerous studies have utilized engineered surfaces to enhance pool boiling heat transfer. In pool boiling, enhancing the heat transfer coefficient can be realized by promoting bubble nucleation with sites that entrap vapor as "seed" for bubbles to grow, and increasing the CHF usually requires a highly wetting surface such that dry-out is delayed. Promoting nucleation can be achieved on an engineered surface by artificially increasing the density of nucleation sites (cavities), reducing substrate wettability, or tuning the cavity sizes. Accordingly, delaying the CHF has been realized by increasing the wettability and roughness of the boiling surface. Figure 1-3 summarizes the pool boiling heat transfer performance (boiling curves) of a few types of engineered surfaces including microchannels, wire mesh, and biconductive, biphilic, surfactant modified, and hydrophilic microstructured or nanostructured surfaces. Compared to the smooth surfaces with intrinsic contact angles of 18°, 35° and 90°, the nanoengineered surfaces showed enhanced heat transfer coefficient (boiling curves shifted to the left) and enhanced CHF (except the surfactant modified surfaces).

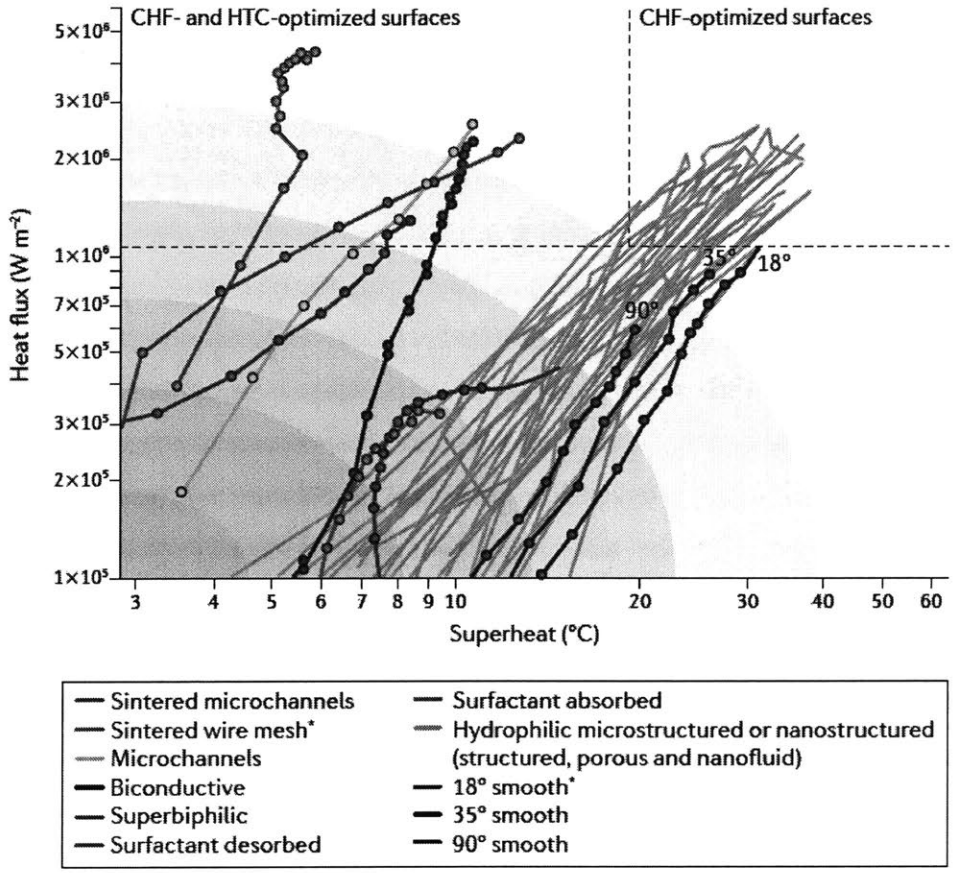

Figure 1-3 Boiling curves up to the CHF for various engineered surfaces, compared to smooth surfaces with contact angles of 18°, 35° and 90°. Figure adapted from Ref. 15

In evaporation, numerous structures have been investigated to enhance the capillary flow and achieve high CHF or dry-out heat flux. Some examples include porous copper structures[16], meshes,[17] silicon micropillar arrays[18,19]. While these studies have suggested exciting potential of using micro and nanostructures to enhance the heat transfer, a detailed model that optimizes the geometries of the structures to enhance the dry-out heat flux is needed.

Recently, inspired by studies of pool boiling and evaporation, surfaces with nanostructures have also been investigated in two-phase microchannels. For example, silicon nanowires have been incorporated into microchannels to reduce temperature oscillation by promoting an early onset of nucleate boiling[20,21], and enhance the CHF.[22,23]

While the focus is on promoting bubble nucleation, the role of surface structures in flow instabilities and CHF needs further investigation, especially at high heat flux conditions.

1.4 Scope and Organization of Thesis

The focus of this thesis is to investigate the role of surface structures in two-phase microchannels and evaporation systems. In particular, we aim to understand the effect of the dimensions of the structures on dry-out heat flux in evaporation systems, and investigate the role of surface structures on flow instabilities and CHF in microchannels.

The thesis is organized as follows. In Chapter 2, a detailed numerical model that predicts capillary-driven liquid flow within micropillar array under a uniform applied heat flux will be presented. The model can be used to determine the dry-out heat flux and optimize the structures for maximizing the dry-out heat flux. In Chapter 3, we integrate surface structures guided by our optimization model into microchannels and investigate their role on CHF and long-timescale (~seconds) flow instabilities prior to CHF conditions. In Chapter 4 we continue to examine short-timescale (~milliseconds) flow instabilities and demonstrate that surface structures that promote capillary flow can significantly suppress the associated temperature oscillations. Chapter 5 summarizes the thesis and suggests future directions based on insights gained from the work presented in previous chapters.

Chapter 2

Dry-out Heat Flux of Capillary Driven Evaporation

Thin-film evaporation in wick structures for cooling high performance electronic devices is attractive because it harnesses the latent heat of vaporization and does not require external pumping. However, optimizing the wick structures to increase the dry-out heat flux is challenging due to the complexities in modeling the liquid-vapor interface and the flow through the wick structures. In this chapter, we developed a model for thin-film evaporation from micropillar array wick structures and validated the model with experiments. The model numerically simulates liquid velocity, pressure, and meniscus curvature along the wicking direction by conservation of mass, momentum and energy based on a finite volume approach. Specifically, the three-dimensional meniscus shape, which varies along the wicking direction with the local liquid pressure, is accurately captured by a force balance using the Young-Laplace equation. The dry-out condition is determined when the minimum contact angle on the pillar surface reaches the receding contact angle as the applied heat flux increases. With this model, we predict the dry out heat flux on various micropillar structure geometries (diameter, pitch and height) in the length scale range of 1-100 μm and discuss the optimal geometries to maximize the dry-out heat flux. We also performed detailed experiments to validate the model predictions, which show good agreement. This model provides insights into the role of surface structures in thin-film evaporation and offers important design guidelines for enhanced thermal management of high-performance electronic devices.

2.1 Background

The increasing power densities in high performance electronic devices such as GaN power amplifiers, concentrated photovoltaics and laser diodes pose a significant thermal management challenge[24–26]. The use of the liquid-to-vapor phase-change process

to cool these devices is attractive because it harnesses the latent heat of vaporization with minimal temperature rise[21,27,28]. In particular, capillary-pumped thin-film evaporation has gained increasing attention due to its simple design, stable and self-regulating performance, and minimal pumping power consumption[13,29,30]. These systems generally require a porous wick structure to generate capillary pressure which drives the liquid flow as it evaporates. Among various wick structures investigated including spheres, pyramids and cylindrical micropillars, the latter have been shown to be a particularly effective wick structure[31]. However, optimizing the micropillars to increase the dry-out heat flux, which is the maximum heat flux the system can dissipate before dry-out occurs, is challenging owing to the complex liquid-vapor interface and its effect on the liquid transport. Thus, existing models simplify the physics by assuming an adiabatic flow[32,33], or neglecting the variation of the three-dimensional curved liquid-vapor interface[34–36] along the length of the wick. In addition, these models are typically based on the Brinkman's equation[32,33,37] or Darcy's law[35,36] which describes flow in an isotropic porous media, with an effective porosity and permeability adopted for the micropillars. Therefore, a multi-physics model, which captures the liquid-vapor interface along the wicking distance and couples the associated capillary pressure field with the fluid and enthalpy transport, is needed for more accurate predictions of the dry-out heat flux.

In this study, we developed a numerical model for thin-film evaporation from micropillar array wick structures. The model simulates the liquid velocity, pressure, and meniscus curvature along the wicking direction by conservation of mass, momentum and energy based on a finite volume approach. In particular, the three-dimensional meniscus shape, which varies along the wicking direction with the local liquid pressure, is accurately captured by the Young-Laplace equation. We determine the dry-out condition at a fixed distance from the liquid source when the minimum contact angle on the pillar surface reaches the receding contact angle as the applied heat flux is increased. We predict the dry-out heat flux on various micropillar structure geometries (diameter d, pitch l, and height h) in the length scale range of 1-100 μm and suggest the optimal geometries to maximize the dry-out heat flux. In addition, we experimentally validated the model with microfabricated test samples and measured the heat flux at which dry-out

occurred. The results show that for the geometric range investigated, the dry-out heat flux is maximized at $d/h \sim 0.4\text{-}0.6$ and $l/d \sim 3$.

2.2Model Formulation

In this work, we study capillary-pumped liquid film evaporation on a hydrophilic micropillar array surface (or the "wick surface") of length L, in a constant pressure, saturated vapor environment. A schematic of the problem studied in this model is shown in Figure 1a (side view) and 1b (top view). Figure 1c shows a scanning electron microscope (SEM) image of a representative fabricated silicon micropillar array with diameter of d, pitch of l and height of h (d, h, $l << L$). The wick surface in Figure 1a and 1b ($0 \leq x \leq L$) is in contact with a liquid reservoir ($x < 0$) at $x = 0$, whose volume is much larger than the total volume of liquid on the wick surface. The wick surface and the liquid in the reservoir are in a saturated environment, with saturated vapor on top. Thus, the pressure of the liquid reservoir (flat interface) is the same as the vapor pressure P_{vap}, which is constant (at P_{sat}) in this system. Upon applying a uniform heat flux q to the bottom of the wick surface, the liquid film evaporates and the film thickness reduces as a function of x. The bottom surface is assumed to be infinitesimally thin such that no axial conduction is present in the solid, which can be large for a thick substrate[38]. However, the liquid-vapor interface is pinned to the hydrophilic micropillar top surfaces. As a result, concave interfaces form (shown in Figure 1a). After the system evolves to equilibrium, the curvature $\kappa(x)$ of this interface increases with x, which is a result of a thinner liquid film further from the reservoir. The liquid pressure $P_{liq}(x)$ is described by the Young-Laplace equation,

$$P_{vap} - P_{liq}(x) = 2\sigma\kappa(x) \tag{2.1}$$

where σ is the liquid-vapor surface tension. For the geometries (1-100 μm) and evaporation conditions studied in this model, the variations of the surface tension with temperature, the disjoining pressure and recoil pressure are negligible. The liquid pressure gradient along x, dP_{liq}/dx, thus results in a net flow from the reservoir (marked by the blue solid arrow in Figure 2-1a), which compensates for the evaporated liquid

mass flux. The goal of this modeling study is to understand the axial variation of the pressure $P(x)$ and the x-direction liquid velocity $U(x)$ at any heat flux q. With this information, we determined the dry-out heat flux $q_{dry\text{-}out}$, as the meniscus curvature at $x = L$ reaches its maximum (*i.e.*, where the liquid-vapor meniscus starts to recede).

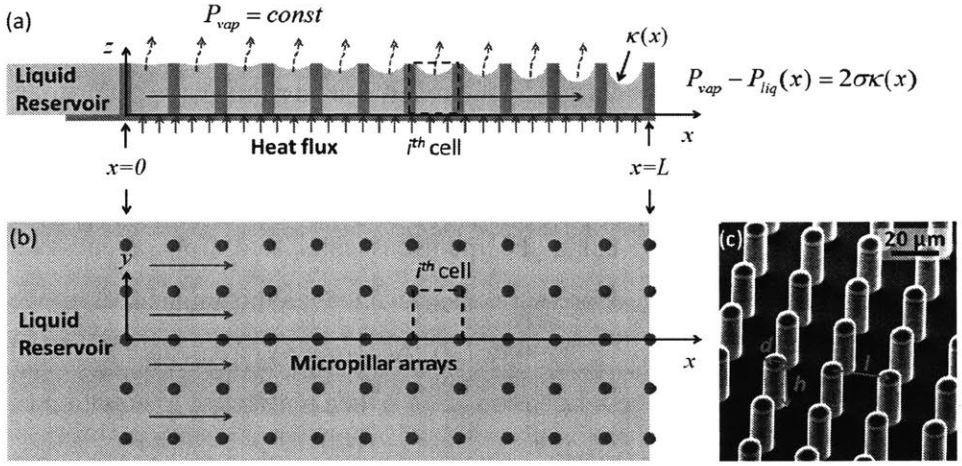

Figure 2-1 (a) Side view and (b) top view schematics of the physical domain in this model. Capillary-pumped liquid film evaporates on a hydrophilic micropillar array surface of length L, where a uniform heat flux is applied. The vapor pressure P_{vap} is constant. The Young-Laplace equation is given, where σ is the liquid-vapor surface tension and $\kappa(x)$ is the curvature of the liquid-vapor interface at any x. (c) A representative SEM image of a fabricated silicon micropillar array with diameter d, pitch l and height h.

Since the micropillars are periodic with pitches of l, we divide the liquid domain into finite volumes or unit cells. Each unit cell is the fluid volume within four pillars shown in the dotted box in Figure 2-1. Since the flow pattern is identical for any finite volume with the same x (i.e., the system is periodic in the y direction), we only consider one row of unit cells. We first consider the meniscus shape in one unit cell from the Young-Laplace equation, and solve for the velocity field in one unit cell using a CFD model. We then link all of the cells from $x = 0$ to $x = L$ based on a finite volume approach where we analyze the change of liquid enthalpy and mass flow rate across a finite volume, and match the mass flux and enthalpy flux for adjacent cells.

2.2.1Force Balance

We first solve for the meniscus shape at an arbitrary unit cell along x with the liquid pressure $P_{liq}(x)$. The curvature of the meniscus in one unit cell is governed by the Young-Laplace equation (equation (2.1)). Since P_{vap} is constant, we define $P_{r,liq}$ as the liquid pressure relative to the vapor pressure, $P_{r,liq} = P_{liq} - P_{vap}$. In the scenarios of practical interest, L is usually much greater than l. It is therefore reasonable to assume that the pressure and curvature variations in one unit cell are small, which we will later validate. Under this condition ($L>>l$), the meniscus in the i^{th} cell which is governed by $\kappa(x)$ or $P_{r,liq}(x)$ is approximated using the meniscus calculated from a cell-averaged curvature κ^i (or the cell-averaged pressure $P_{r,liq}{}^i$), since in this numerical model we discretize the pressure $P_{r,liq}(x)$ as $P_{r,liq}{}^i$ (i=0 to L/l). Accordingly, we denote x', y' and z' as the relative coordinates in a unit cell. Equation (2.1) is then rearranged to equation (2.2).

$$\kappa^i = \frac{-P_{r,liq}{}^i}{2\sigma} \tag{2.2}$$

The curvature of a 3-D surface $z' = f(x',y')$ is calculated as,

$$2\kappa^i = -\nabla \cdot \hat{n} \tag{2.3}$$

where $\hat{n}$ is the unit normal of the surface defined as equation (2.4)[39].

$$\hat{n} = \frac{\left(\frac{\partial f}{\partial x'}, \frac{\partial f}{\partial y'}, -1\right)}{\left(\left(\frac{\partial f}{\partial x'}\right)^2 + \left(\frac{\partial f}{\partial y'}\right)^2 + 1\right)^{1/2}} \tag{2.4}$$

Given any $P_{r,liq}{}^i$, the constant-mean-curvature (CMC) meniscus shape $z' = f_{meniscus}(x',y')$ is numerically computed using equation (2.3) and (2.4) in COMSOL[40] by setting $\kappa^i = -P_{r,liq}{}^i/(2\sigma)$.

The boundary conditions (before the meniscus starts to recede within the unit cell) are: a) the interface is pinned at the pillar top,

$$z' = h \text{ at } \begin{array}{l} x'^2 + y'^2 = (d/2)^2, \\ (x'-l)^2 + y'^2 = (d/2)^2, \\ x'^2 + (y'-l)^2 = (d/2)^2, \\ (x'-l)^2 + (y'-l)^2 = (d/2)^2, \\ 0 \le x', y' \le l \end{array} \tag{2.5}$$

and b) the slope of the meniscus where adjacent cells meet is continuous. More specifically, the slope in the x' direction should be zero at $x' = 0$ and l, when the pressure difference between adjacent cells is infinitesimally small, and the slope in the y' direction is zero at $y' = 0$ and l, due to symmetry.

$$\frac{\partial z'}{\partial x'} = 0 \text{ at } x' = 0, l \text{ and } \frac{\partial z'}{\partial y'} = 0 \text{ at } y' = 0, l \tag{2.6}$$

Due to the various geometries simulated (1-100 μm), we used a standard optimized mesh generation algorithm in COMSOL[40] to generate the grid. The minimum and maximum relative mesh areas (with respect to the unit cell projected area) were approximately 1×10^{-5} and 7×10^{-5}. The relative tolerance for the convergence of z' was 10^{-6}. The results were exported in the form of points (x', y', z'). The mesh independence of the numerical solution is included in Figure 2-3.

An example of the meniscus in a unit cell (d=3 μm, l=9 μm, h=5 μm) with $\kappa^i = 5.52\times10^{-2}$ μm^{-1} which corresponds to $P_{r,liq} = -6.49$ kPa (σ = 58.8 mN/m, water at 100 °C) is shown in Figure 2-2a. We choose water due to its large latent heat of vaporization compared to other fluids. From the meniscus solution, we further obtain the contact angle θ that the meniscus makes on the pillar surface (Figure 2-2c).

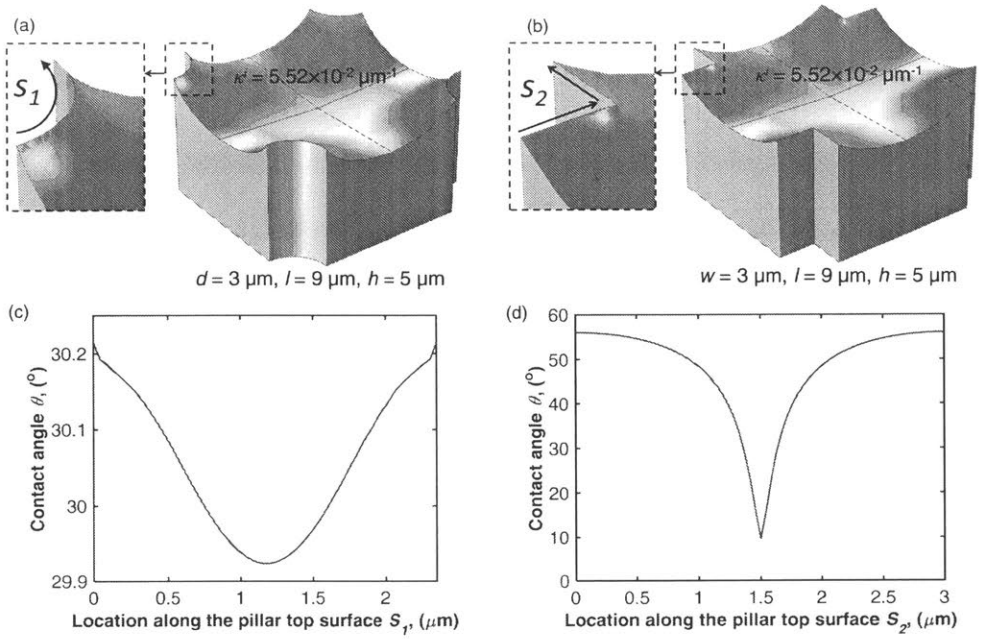

Figure 2-2 (a) The meniscus shape for (a) cylindrical pillar arrays with d = 3 μm, l = 9 μm, h = 5 μm and $\kappa^i = 5.52\times10^{-2}$ μm^{-1}, (b) rectangular pillar arrays with width w = 3 μm, l = 9 μm, h = 5 μm and $\kappa^i = 5.52\times10^{-2}$ μm^{-1}, computed from equation (2.3) and (2.4) in COMSOL. The menisci are assumed to be pinned (i.e., the contact angle is larger than the receding contact angle). The corresponding contact angle around a quarter of a (c) cylindrical micropillar and (d) rectangular micropillar, respectively.

The contact angle varies around the pillar circumference ($29.92° < \theta < 30.21°$, Figure 2-2c) as expected due to the non-axisymmetric geometry and interactions with the adjacent three pillars, but this variation is small for cylindrical micropillar geometries with reasonably large permeability which is of practical interest in wicking applications. In this case, the corresponding average contact angle obtained from the meniscus solution around a pillar is $\theta = 30.06°$, which matches very well with the average contact angle ($\theta = 30.00°$) calculated from a force balance analysis described by equation (2.7),

$$\sigma(\pi d)\cos\theta = -P_{r,liq}(l^2 - \pi r^2) \tag{2.7}$$

where r ($r = d/2$) is the radius of the pillar. The left hand side of equation (2.7) represents the vertical component of the line forces pulling the meniscus upward. The right hand side of equation (2.7) is the downward component of the force from the pressure difference acting on the meniscus.

It is to be noted that the contact angle non-uniformity can be significant around a pillar top surface for shapes other than cylindrical micropillars, especially for those shapes with sharp corners (*e.g.*, rectangular). The contact angle non-uniformity can result in a partial receding and partial pinning state of the meniscus, and the calculation of such intricate meniscus shape will need further consideration. For example, the contact angle around a square micropillar (widths $w = 3$ μm, pitch $l = 9$ μm) with the same curvature ($\kappa^i = 5.52\times10^{-2}$ μm^{-1}) is significantly non-uniform (from 9° to 56°), assuming the meniscus is pinned (Figure 2-2b and d). This means that if the receding contact angle is 15°, for example, the assumption that the meniscus is pinned around the pillar before the dry-out heat flux occurs is not valid. In this case, part of the three-phase contact line will recede first while part of it is pinned. Since the dry-out heat flux is determined by the receding of the entire contact line, obtaining the dry-out heat flux will require accurate calculation of this intermediate partially receding meniscus as well as integration of this meniscus into the CFD model. In this thesis we will only consider cylindrical micropillar arrays as they are more common in scalable structures.

Figure 2-3 shows an example of the average meniscus height and minimum meniscus height of the center *yz*-plane in a unit cell (the red plane in the inset of Figure 2-3) as a function of the contact angle θ (d=3 μm, l=9 μm, h=5 μm), or curvature κ. The result shows that, for this particular pillar geometry, the liquid-vapor interface curves towards the bottom surface for ~40% the total height of the pillar at small contact angles. This indicates that assuming the liquid thickness is equal to the micropillar height can largely underpredict the flow resistance, especially for small h/l ratio geometries. Following the same method, we solved the meniscus shape for various pillar geometries and $P_{r,liq}$ (or κ) using a parametric sweep in COMSOL.

(a) (b)

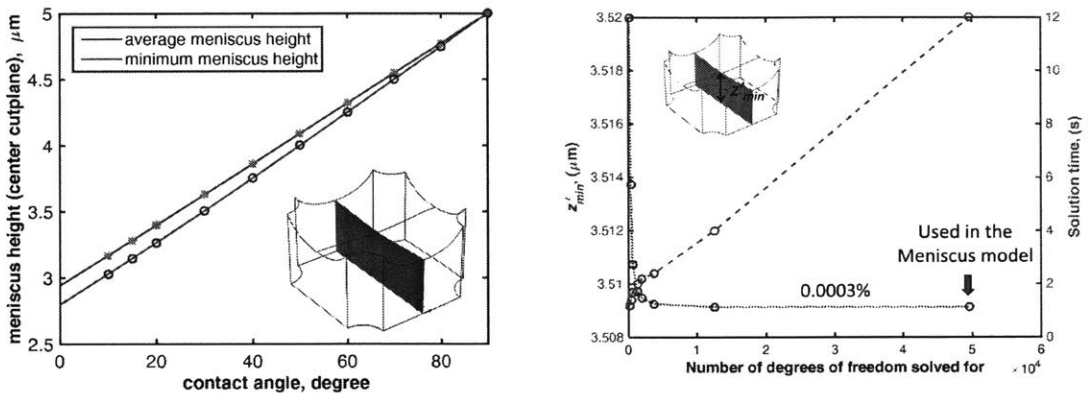

Figure 2-3 (a) the average meniscus height and minimum meniscus height in the center *yz*-plane (the red plane in the inset) of a unit cell (d = 3 μm, l = 9 μm, h = 5 μm) as a function of the average contact angle θ around the pillars. The solid lines are linear interpolation and extrapolation of the data points from COMSOL. (b) The meniscus height z'_{min} at the center of a unit cell (d = 3 μm, l = 9 μm, h = 5 μm, θ = 30°) and the solution time as a function of the total number of degrees of freedom solved for (as a result of different mesh sizes) in the COMSOL model for meniscus calculation. The blue arrow indicates the solution used in this mode. The difference in z'_{min} between the last two data points is 0.0003%.

2.2.2 Momentum Equation

We next solve the momentum equation (Navier-Stokes Equations) for the velocity field (u,v,w) in one unit cell as a function of the relative liquid pressure $P_{r,liq}$ which determines the meniscus shape, and the pressure difference across one unit cell $\Delta P_{r,liq}/l$ which drives the flow. Due to the complexity of the meniscus shape, we solve the three-dimensional velocity profile $(u,v,w) = f(P_{r,liq}, \Delta P_{r,liq}/l, x', y', z',$ micropillar geometries) numerically *via* CFD simulations in COMSOL. We imported the meniscus shape (x', y', z') calculated in the previous section *via* parametric surface in COMSOL as a geometric boundary. We choose the fluid properties of water at 100 °C. Figure 2-4a shows an example of a unit cell (d = 3 μm, l = 9 μm, h = 5 μm). For any input $P_{r,liq}$, the meniscus is first generated by the method described in the previous section. A pressure difference $\Delta P_{r,liq}$ is applied across the inlet and the outlet of the fluid domain, which represents a cell-averaged pressure gradient $dP_{r,liq}/dx \approx \Delta P_{r,liq}/l$. The boundary conditions are a) no-slip boundary condition on the bottom surface and the pillar side walls, b) shear free

boundary condition on the meniscus and c) symmetric boundary condition on the side walls of the unit cell ($y = 0$ plane and $y = l$ plane). The minimum and maximum relative mesh volumes (with respect to the unit cell volume) were approximately 1×10^{-6} and 1.5×10^{-4}. The relative tolerance for the convergence of velocity and pressure was 10^{-3}. Figure 2-4a shows the result of the magnitude of the velocity (m/s) in the fluid domain where $P_{r,liq} = -6.49$ kPa which corresponds to $\kappa^i = 5.52\times10^{-2}$ μm^{-1} or $\theta = 30°$, and a $\Delta P_{r,liq}/l$ of −1.667 Pa/μm ($\Delta P_{r,liq} = -15$ Pa over $l = 9$ μm). The mesh independence of the numerical solution is included in Figure 2-5.

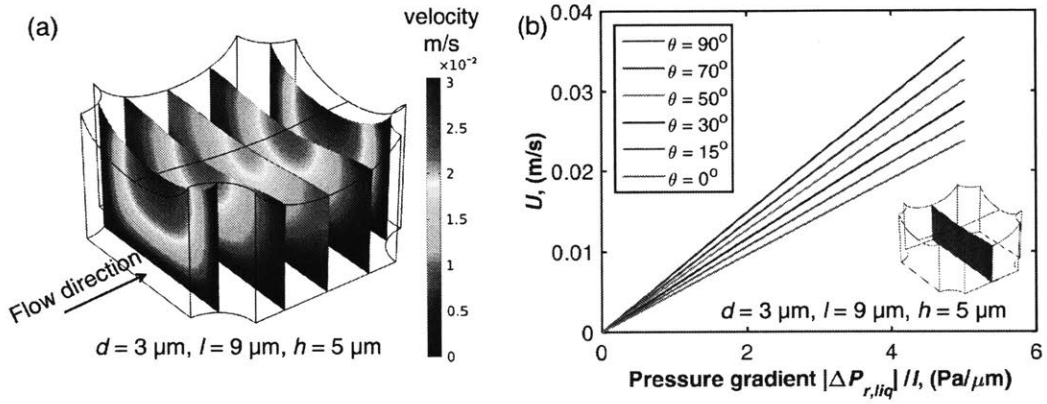

Figure 2-4 (a) The magnitude of the velocity (m/s) in the fluid domain where $P_{r,liq} = -6.49$ kPa which corresponds to $\kappa^i = 5.52\times10^{-2}$ μm^{-1} or $\theta = 30°$, and a $\Delta P_{r,liq}/l$ of −1.667 Pa/μm ($\Delta P = -15$ Pa over $l = 9$ μm). The micropillar geometries are $d = 3$ μm, $l = 9$ μm, $h = 5$ μm. (b) The center-yz-plane-averaged (the red plane in the inset) x-direction velocity U defined as $U = \frac{1}{A_c}\iint_{A_c} u(x',y',z')dy'dz'\big|_{x'=l/2}$ as a function of $|\Delta P_{r,liq}|/l$ and $\theta = f(P_{r,liq})$.

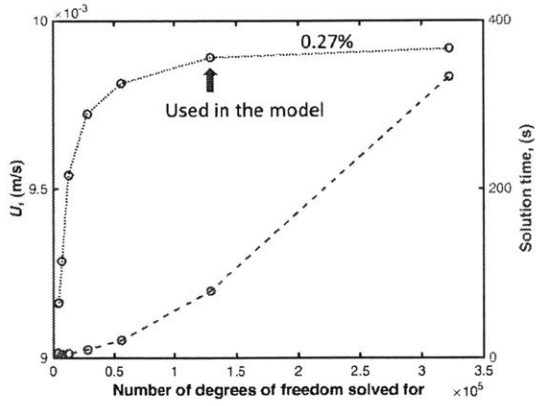

Figure 2-5 The center-yz-plane averaged velocity U and the solution time as a function of the total number of degree of freedom solved for in the CFD model, with

a micropillar geometry of $d = 3$ μm, $l = 9$ μm, $h = 5$ μm, a contact angle of $\theta = 30°$ and an applied pressure difference of 15 Pa. The blue arrow indicates the solution used in this model. The difference in U between the last two data points is 0.27%.

We performed simulations over a wide range of values for pressure gradient $\Delta P_{r,liq}/l$ and pressure $P_{r,liq}$, to obtain their effect on the liquid velocity. The result for $d = 3$ μm, $l = 9$ μm, $h = 5$ μm is plotted in Figure 2-4b where the center-yz-plane-averaged (the red plane in the inset) x-direction velocity U (defined as $U = \frac{1}{A_c}\iint_{A_c} u(x',y',z')dy'dz'\big|_{x'=l/2}$) is shown as a function of $|\Delta P_{r,liq}|/l$ and $\theta = f(P_{r,liq})$. For a fixed contact angle (*i.e.*, a fixed meniscus shape), the result shows a linear relationship between the velocity and the pressure gradient, which is due to a fixed flow resistance. As θ reduces, the meniscus becomes more concave. This increases the flow resistance, as indicated by the reduced slopes of the U *vs.* $|\Delta P_{r,liq}|/l$ curves. Besides $|\Delta P_{r,liq}|/l$ and pressure $P_{r,liq}$, we also performed simulations over a wide range of sample geometries (d, l, h) to obtain a look-up table for $U = f(P_{r,liq}, \Delta P_{r,liq}/l, d, l, \text{h})$. We used this look-up table for the finite volume simulations discussed next.

2.2.3 Mass Conservation and Enthalpy Balance

We finally connect the unit cells from $x = 0$ to $x = L$ by integrating the mass conservation and enthalpy balance equations in each unit cell, or finite volume, and matching the fluxes at the finite volume interfaces. For the convenience of the study, we chose the finite volumes as shown in Figure 2-6, so that the boundaries of the finite volumes coincide with the center yz-planes in each unit cell.

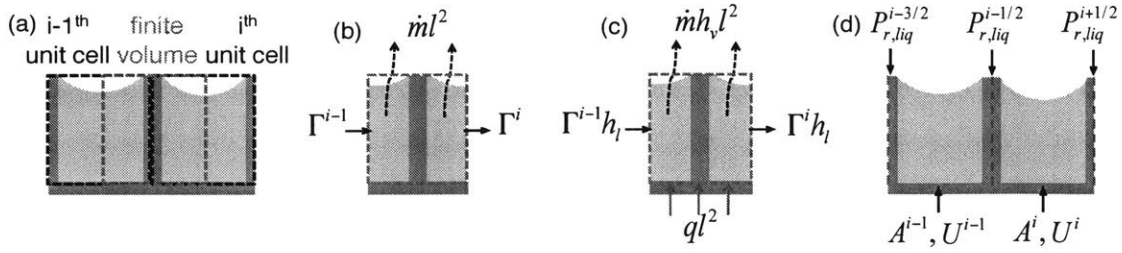

Figure 2-6 Schematics of (a) the choice of finite volume and unit cells, (b) mass conservation and (c) enthalpy balance on a control volume, and (d) locations of the variables solved in the model.

Integrating the mass conservation in the finite volume gives equation (2.8),

$$\Gamma^{i-1} - \Gamma^{i} = \dot{m}l^2 \tag{2.8}$$

where Γ^{i-1} and Γ^{i} represent the mass flow rate entering and leaving the finite volume respectively, and $\dot{m}$ is the evaporation rate (*i.e.*, the mass evaporated per unit area per second, kg/m^2·s). Γ^{i} is calculated by integrating the mass flux on the outlet surface and is described by equation (2.9),

$$\Gamma^{i} = \rho \iint_{A^i} u dy dz = \rho A^i U^i \tag{2.9}$$

where ρ is the liquid density, u is the x-direction velocity, A^i is the outlet surface area which is also the center yz-plane area A_c in a unit cell, and U^i is the surface-averaged velocity (as discussed in Section 2.2.2). A similar equation is used to calculate Γ^{i-1}.

Integrating the enthalpy in the finite volume gives equation (2.10),

$$(\Gamma^{i-1} - \Gamma^{i})h_l - \dot{m}l^2 h_v + l^2 q = 0 \tag{2.10}$$

where h_l and h_v are the enthalpies of the liquid and vapor respectively. Substituting equations (2.8) and (2.9) into (2.10), and neglecting the sensible heat results in equation (2.11),

$$\rho(A^{i-1}U^{i-1} - A^i U^i)h_{fg} = l^2 q \tag{2.11}$$

where h_{fg} is the latent heat of vaporization (h_v-h_l).

The boundary conditions at $x = 0$ are a) $P_{r,liq} = 0$ since the liquid is in contact with the reservoir, and b) $\Gamma(x = 0) = qlL/h_{fg}$ since all the liquid evaporated from the surface should enter at $x = 0$. Equation (2.11) links the center-yz-plane-averaged velocity U^i and the area A^i with those in the next unit cell. Therefore, we solved $P_{r,liq}$ based on a cell-by-cell (forward) approach, since the left boundary conditions ($x = 0$) are specified. Based on the solution from the previous cell ($P_{r,liq}^{\ i-1/2}$, A^{i-1}, U^{i-1}) whose locations are defined in Figure 2-6d, $P_{r,liq}^{\ i+1/2}$ is iteratively solved until $A^i = f(P_{r,liq}^{\ i})$ and $U^i = f(P_{r,liq}^{\ i}, (P_{r,liq}^{\ i+1/2} - P_{r,liq}^{\ i-1/2})/l)$ satisfies equation (2.11), where $P_{r,liq}^{\ i}$ is the average pressure in the i^{th} cell and $P_{r,liq}^{\ i} = 1/2(P_{r,liq}^{\ i-1/2} + P_{r,liq}^{\ i+1/2})$. The solution ($P_{r,liq}^{\ i+1/2}$, A^i, U^i) is then used to calculate ($P_{r,liq}^{\ i+3/2}$, A^{i+1}, U^{i+1}) in the next cell.

2.3 Results and Discussion

In this section, we first show an example of the solution of a micropillar array surface ($d = 10$ μm, $l = 30$ μm, $h = 25$ μm) of length $L = 5$ mm. We choose this characteristic wicking length L based on a 1 cm^2 typical heat dissipation area of electronic devices, where the fluid wicks from the edges to the center. We discuss how we obtain the dry-out heat flux $q_{dry\text{-}out}$ based on the minimum contact angle from the solution. We then show the dry-out heat flux $q_{dry\text{-}out}$ for various micropillar geometries as the pillar height h increases from 5 μm to 50 μm and discuss the optimal pillar geometries which maximize $q_{dry\text{-}out}$. Furthermore, we validate this model with experimental data and demonstrate good agreement between the two. Finally, we show that $q_{dry\text{-}out}$ is very sensitive to the wicking length L and is governed by $q_{dry\text{-}out} \sim L^{-2}$.

2.3.1 Solution of a representative micropillar surface

Figure 2-7 shows the x-direction velocity $U(x)$ (Figure 2-7a), the relative liquid pressure $P_{r,liq}(x)$ (Figure 2-7b), the average meniscus height (liquid thickness) in the center yz-plane in each unit cell $\delta(x) = A_c(x)/l$ (Figure 2-7c), and the average contact angle that the meniscus makes on the micropillar walls $\theta(x)$ (Figure 2-7d) as a function of the distance x to the reservoir. Three heat fluxes $q = 50$, 60 and 76.1 W/cm^2 were applied and the dashed arrows in Figure 2-7 indicate the trend as the heat flux increases. The heat flux of 76.1 W/cm^2 corresponds to the dry-out heat flux which will be explained in the following paragraph. Figure 2-7a shows that the velocity reduces to zero at $x = L$, which is a physical result of total evaporation of the liquid. This also indicates that the error associated with the numerical method is small, since we only specified the left boundary conditions at $x = 0$ and did not set any constraints at $x = L$. Figure 2-7b shows that $P_{r,liq}$ reduces along the wick surface and the magnitude of the total pressure drop increases with q. In addition, the maximum pressure variation within a unit cell at q = 76.1 W/cm^2 is 23.9 Pa (at $x = 0$), which is only 1% of the pressure variation from $x = 0$ to L (−2.17 kPa). This validates our previous assumption that the pressure variation in one unit cell is small. Figure 2-7c and d shows that the thickness of the liquid film and the average contact angle reduces along the wick surface. As heat flux increases, the liquid becomes thinner and the contact angle reduces.

We identify the dry-out heat flux $q_{dry\text{-}out}$ by the physical constraint of the minimum contact angle at $x = L$. This contact angle cannot be lower than the receding contact angle θ_r of the fluid on the substrate. Similarly, the receding contact angle has been used to identify the critical heat flux in pool boiling [41,42]. As an example of water on silicon dioxide, which is a common combination, θ_r is approximately 15° [43]. Thus $q_{dry\text{-}out}$ in this particular case is determined to be 76.1 W/cm^2, as shown in Figure 2-7d.

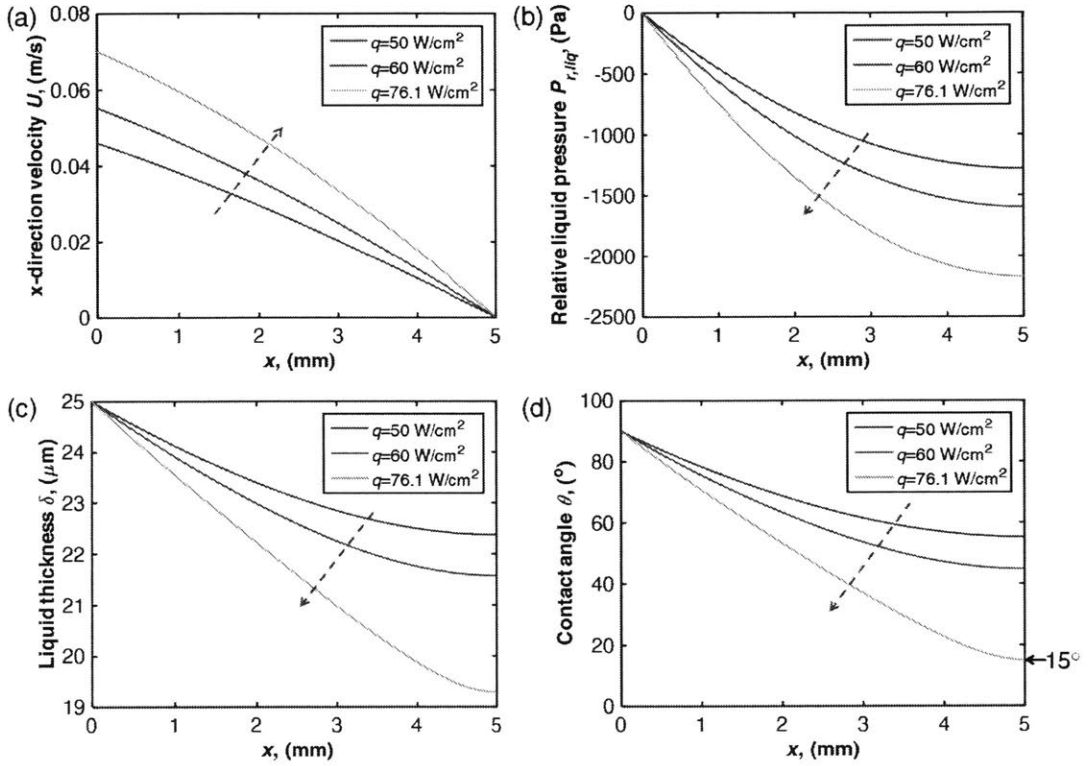

Figure 2-7 A representative set of simulation results for a micropillar array surface ($d = 10$ μm, $l = 30$ μm, $h = 25$ μm) of length $L = 5$ mm at $q = 50$, 60 and 76.1 W/cm^2. (a) The x-direction velocity $U(x)$, (b) the relative liquid pressure $P_{r,liq}(x)$, (c) the average meniscus height (liquid thickness) in the center yz-plane in each unit cell $\delta(x) = A_c(x)/l$, and (d) the average contact angle that the meniscus makes on the micropillar walls $\theta(x)$ as a function of the distance x to the reservoir. Water (at 100 °C) is used as the working fluid.

2.3.2 Dry-out Heat Flux for Various Micropillar Geometries

Following the method described in section 2.3.1, we calculated the dry-out heat flux $q_{dry\text{-}out}$ for various micropillar geometries and the results are shown in Figure 2-8.

Micropillars of three different heights (h = 5 μm, 25 μm and 50 μm) which correspond to three inlet liquid thickness were investigated. For each h, we examined the micropillar diameters d in the range of approximately d/h~0.1 to 1. Correspondingly, various micropillar pitches l were considered such that for each d and h, the range of l covers the maximum $q_{dry\text{-}out}$. Figure 2-8(a-c) show $q_{dry\text{-}out}$ for h = 5 μm, 25 μm and 50 μm respectively when θ_r = 15° (water on silicon dioxide). Figure 2-8d shows $q_{dry\text{-}out}$ for h = 25 μm when θ_r = 50° (representing the case for pillar surfaces with a lower surface energy). The numerical error associated with discretization increases as L/l decreases. Specifically, the number of unit cells becomes less than 50 for l > 100 μm (L = 5 mm), and the maximum pressure variation within a unit cell at dry-out (θ_r = 15°) for d = 50 μm, l = 100 μm and h = 50 μm increases to 3.6% (40.4 Pa at x = 0) of the total pressure variation from x = 0 to L (−1.11 kPa).

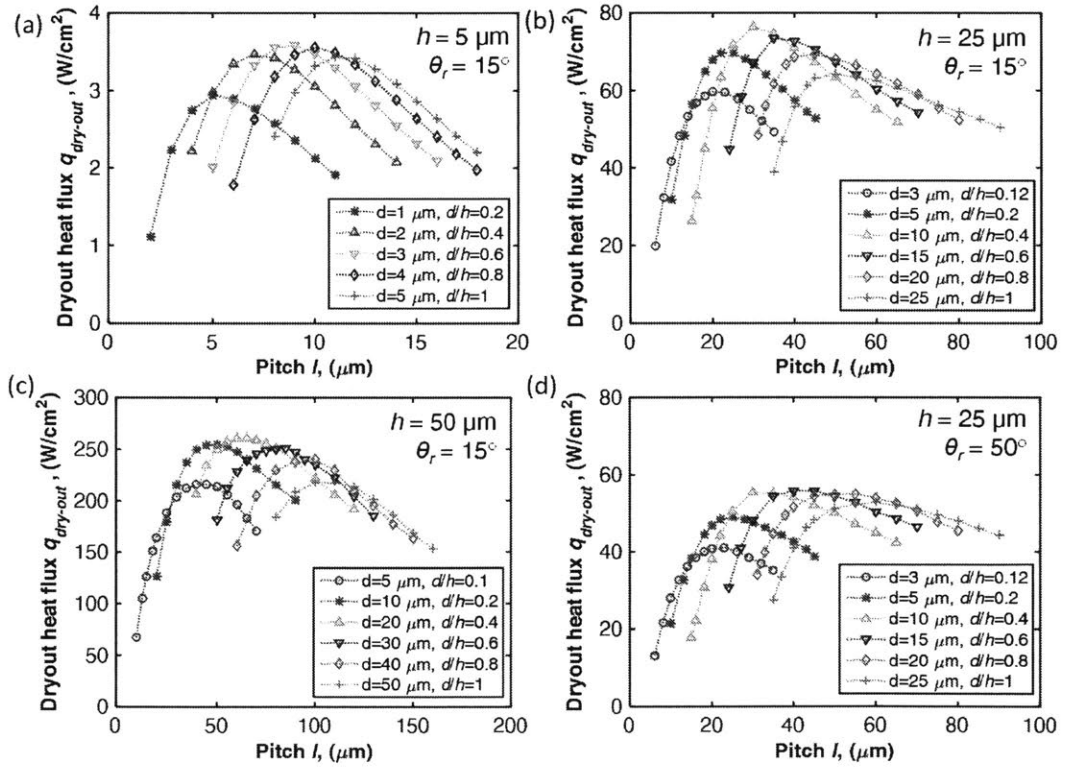

Figure 2-8 The dry-out heat flux $q_{dry\text{-}out}$ for various micropillar geometries. (a) h = 5 μm and θ_r = 15°, (b) h = 25 μm and θ_r = 15°, (c) h = 50 μm and θ_r = 15°, and (d) h = 25 μm and θ_r = 50°.

The results indicate the dry-out heat flux is very sensitive to the choice of the micropillar geometries. We summarize the main observations from these simulations over the parametric space as seen in Figure 2-8,

(1) For each h, there is a maximum $q_{dry\text{-}out}$, and for the geometries investigated in this study, the optimal geometry has a d/h ratio of approximately 0.4-0.6, and an l/d ratio of approximately 3 when $\theta_r = 15°$.

(2) $q_{dry\text{-}out}$ increases with h. This is because higher h results in a thicker liquid film and the associated viscus drag ($\sim\mu \cdot du/dz$) from the bottom surface is smaller. In addition, a thicker liquid allows a higher liquid mass flow rate, which contributes to a higher $q_{dry\text{-}out}$. This trend agrees with previous modeling based on the Darcy's equation and experimental observations [35,36]. However, increasing the height of the pillars increases the superheat at the solid surface. Therefore, h is limited by the maximum superheat associated with the onset of nucleation, which needs further consideration. Due to this boiling limit, we do not report $h > 50$ μm, since a mixed mode of evaporation and boiling has been observed from some previous works [19,29,44] for geometries in this range. Similarly, when the contact angle is large, it is also possible for boiling to occur due to the small evaporative heat transfer coefficient[45].

(3) Reducing θ_r will increase $q_{dry\text{-}out}$, as indicated by Figure 2-8b and d.

2.3.3 The Effect of Receding Contact Angle on the Dry-out Heat Flux

To further investigate the effect of the receding contact angle on the dry-out heat flux, we plot $q_{dry\text{-}out}$ as a function of θ_r for three different micropillar geometries. Figure 2-9 suggests that although the dry-out heat flux increases with decreasing receding contact angle, the increase is small as θ_r approaches 0°. This relation resembles $q_{dry\text{-}out} \sim \cos\theta_r$ since the maximum capillary pressure is $-P_{r,liq} = \cos\theta_r \sigma(\pi d)/(l^2 - \pi r^2)$, according to equation (2.7). The exact $q_{dry\text{-}out} = f(\theta_r)$ is micropillar geometry dependent, as indicated by the difference between the curves for $l = 60$ μm and $l = 20$ μm in Figure 2-9. The predictions for $l = 60$ μm are higher than that for $l = 20$ μm at larger receding contact angles, but becomes lower at receding contact angles less than 21°. This is because as the contact angle decreases the liquid film becomes thinner for sparse pillar arrays compared

to micropillars with relatively closer spacing (insets of Figure 2-9), which causes more viscous drag. This result explains the trend that the optimal d and l increase as θ_r increases (Figure 2-8b and d). In addition, creating nanoscale hierarchical structures on top of the microscale pillar arrays can potentially reduce the apparent contact angle on the pillar surface to zero degree. Although this can increase the maximum allowable capillary pressure, the additional viscous loss introduced by the rough nanostructures may introduce additional viscous resistance. Predicting the dry-out heat flux needs consideration of both factors.

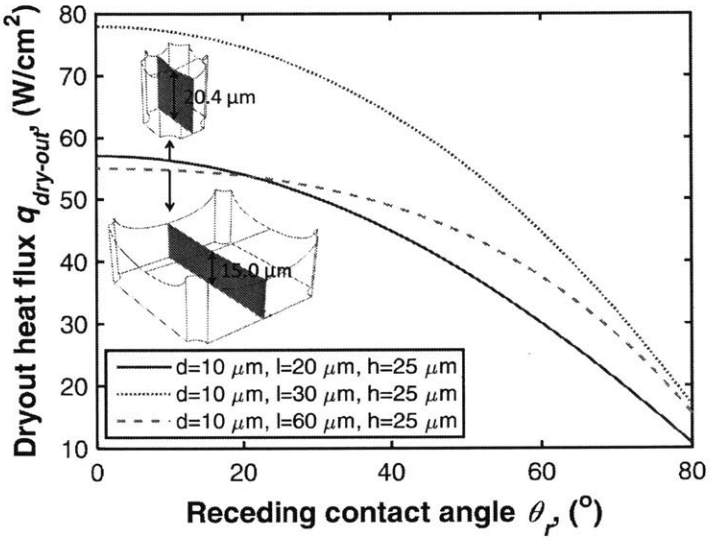

Figure 2-9 The dry-out heat flux as a function of the receding contact angle for three different micropillar geometries. The dry-out heat flux increases as the receding contact angle decreases. The insets show the minimum liquid film thicknesses for a sparse and dense pillar arrays (h = 25 μm) with θ_r = 10°.

2.3.4 Experimental Validation and the Effect of Wicking Length

We validated our model with experimental data. We created well-defined micropillar arrays with three geometries (Sample A1: d = 7 μm, l = 20 μm, h = 20 μm, A2: d = 7 μm, l = 30 μm, h = 19 μm and A3: d = 6 μm, l = 50 μm, h = 19 μm). Sample A1 and A2 are around the optimal geometry for h ~ 20 μm and A3 is non-optimized. The micropillars were etched on a silicon substrate (~600 μm thick) *via* deep reactive ion etching and a thin thermal oxide (~50 nm) is grown to ensure that the surface is wetting.

The scanning electron microscopy (SEM) images of the fabricated micropillars are shown in Figure 2-10.

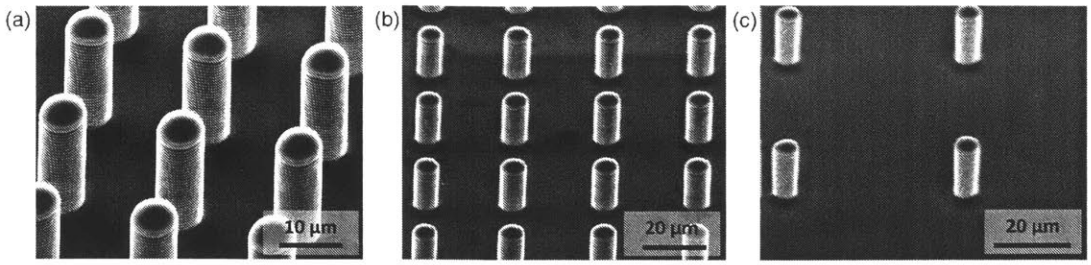

Figure 2-10 SEM images of the fabricated silicon micropillar arrays. (a) Sample A1: $d = 7$ μm, $l = 20$ μm, $h = 20$ μm, (b) Sample A2: $d = 7$ μm, $l = 30$ μm, $h = 19$ μm and (c) Sample A3: $d = 6$ μm, $l = 50$ μm, $h = 19$ μm.

The schematic of the sample is shown in Figure 2-11a. Each sample was 2 cm × 2.5 cm × 600 μm. Micropillars were patterned on the samples with a width of 10 mm and length of L+1 mm, where L is the wicking length. Samples with five different wicking distances L (5-10 mm) were fabricated. The structured area is 2 mm above the bottom edge of the sample. A thin-film heater was patterned on the backside of the sample, with an area of 10 mm × L mm. Three thin-film resistive temperature sensors were also patterned on the backside of the sample.

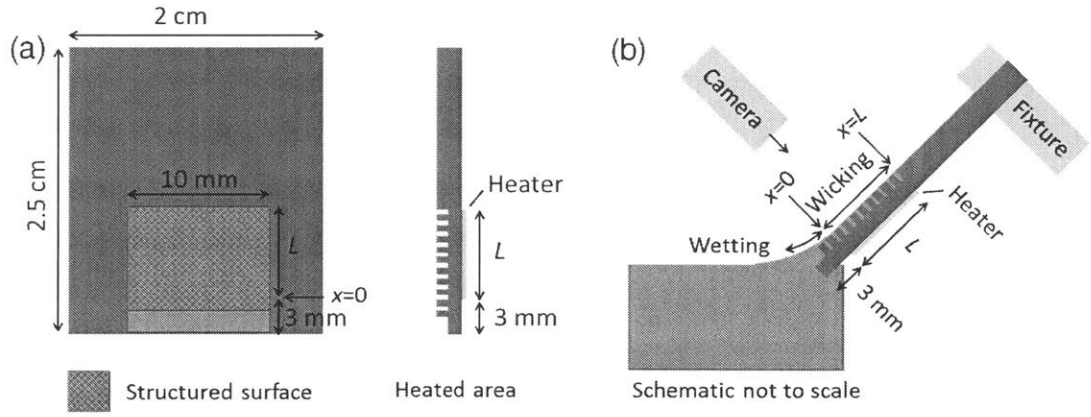

Figure 2-11 (a) Schematic of the front and side view of the fabricated sample. (b) Schematic of the experimental setup.

Prior to the experiment, the samples were rinsed in acetone, isopropyl alcohol and de-ionized water, and subsequently plasma cleaned in an oxygen environment for 15 minutes to remove any surface contamination. The schematic of the experimental setup is

shown in Figure 2-11b. For all experiments, the sample was placed in a custom Ultem fixture which was connected to a *z*-stage. The sample was tilted 45° and brought into contact with a reservoir filled with de-ionized water in order to ensure that the liquid propagation is only *via* wicking. The bulk fluid wetted the bottom of the sample (Figure 2-11) upon contact due to surface tension. A camera was used to facilitate visualization of the wicking region. The z-stage was adjusted such that the wicking region matched with the heater area. The extra 1 mm structured surface area ensured liquid supply from the reservoir in case of wetting region fluctuation.

During the experiment, we heated the sample in the ambient environment (P = 1 atm) by a power supply controlled by LabVIEW. We increased the heat flux in small increments (1~2 W/cm^2) such that at each heat flux, the system operated for approximately 60 s (the rise time for the temperature to reach steady state when the heat flux was incremented was approximately 10 s). We obtained the dry-out heat flux when the liquid at $x = L$ started to recede. The total heat flux was calculated using the input power divided by the heater area A_{heater} = 10 mm × L. We also calibrated the heat loss *via* conduction and convection into the liquid reservoir by using a non-wetting surface (no hydrophilic structures on the front side) and measured the heater input power as a function of the sample temperature. The evaporative heat flux q was calculated by equation (2.12),

$$q = \frac{P_{input}}{A_{heater}} - \frac{P_{loss}}{A_{heater}} \tag{2.12}$$

We compared the measured $q_{dry\text{-}out}$ (Figure 2-12a) as a function of L with the model (θ_r = 15°). The experimental data shows good agreement with the model.

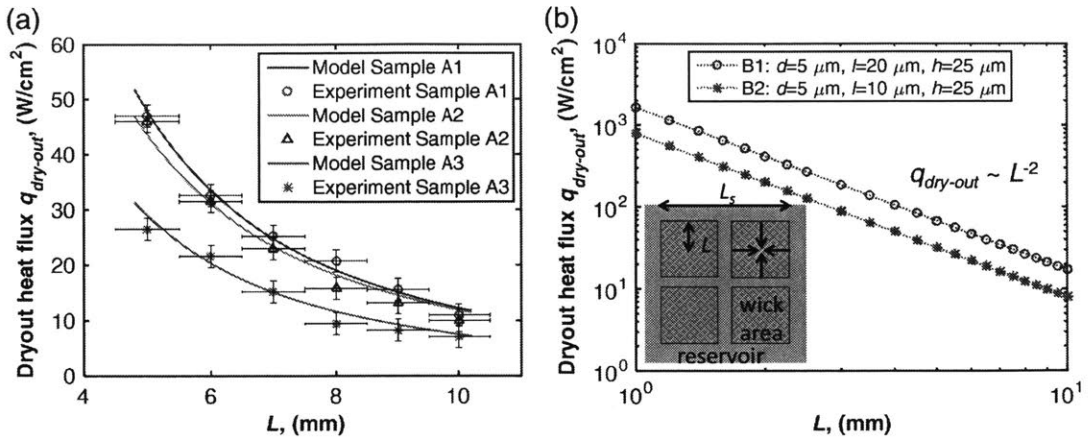

Figure 2-12 (a) Experimental data and model of $q_{dry-out}$ *vs.* L on three wick geometries (A1: $d = 7$ μm, $l = 20$ μm, $h = 20$ μm, A2: $d = 7$ μm, $l = 30$ μm, $h = 19$ μm and A3: $d = 6$ μm, $l = 50$ μm, $h = 19$ μm) with different wicking length L. $\theta_r = 15°$. (b) The dry-out heat flux $q_{dry-out}$ as a function of the wick surface length L as predicted by the model for two micropillar geometries (B1: $d = 5$ μm, $l = 20$ μm, $h = 25$ μm and B2: $d = 5$ μm, $l = 10$ μm and $h = 25$ μm) with $\theta_r = 15°$. Inset is a schematic showing a design that extends the reservoir region to the heat transfer surface by incorporating channels with minimal pressure drop from the main reservoir.

Finally, we discuss the effect of the wicking length L on $q_{dry-out}$, and show the importance of L, aside from the microstructure geometries, in capillary-pumped heat sink designs. Figure 2-12b shows $q_{dry-out}$ as a function of L based on our model for two micropillar geometries (Sample B1: $d = 5$ μm, $l = 20$ μm, $h = 25$ μm and B2: $d = 5$ μm, $l = 10$ μm and $h = 25$ μm). B1 is chosen close to the optimal micropillar geometries for $h = 25$ μm and B2 has non-optimized geometries (see Figure 2-8b). The dependence of $q_{dry-out}$ *vs.* L on a log-log scale appears linear which indicates a power law relationship between the two. In fact, the slopes in Figure Figure 2-12b suggest that $q_{dry-out} \sim L^{-2}$. The physical reason behind this relationship is because $q_{dry-out} \times L$ scales with the total heat input Q to the surface, and $Q \propto \Gamma(x = 0) \propto P_{cap,max}/L$, where Γ is the liquid mass flow rate (equation (2.9)) and $P_{cap,max}$ is the maximum capillary pressure for a given micropillar geometry. Figure 2-12b indicates that, although the two geometries B1 and B2 lead to ~100% difference in $q_{dry-out}$ for the same L (see Figure 2-8), $q_{dry-out}$ spans two orders of magnitude when L is varied from 1 mm to 10 mm. This suggests that: 1) It is possible to achieve a significant heat flux only over a small area, however this does not necessarily correspond to an optimized wick surface. 2) Achieving high heat fluxes as the wick

surface scales up is difficult, since $q_{dry\text{-}out}$ quickly decreases with L^2. However it is possible to extend the reservoir region to the heat transfer surface by incorporating channels with minimal pressure drop from the main reservoir (inset of Figure 2-12b). The channels needs to be designed such that liquid flow can be sustained (i.e., dry-out cannot occur in the channels prior to the structures). This offers an opportunity to further enhance the dry-out heat flux by reducing the characteristic wicking length L while still increasing the total heat transfer surface length L_s (*i.e.*, $L_s > L$).

In conclusion, we have demonstrated a modeling framework to predict thin film evaporation in micropillar wick surfaces and we validated the model with experimental data. The model accurately captures the effect of the three-dimensional meniscus shape, which varies along the wicking direction, by solving the Young-Laplace equation. Dry-out heat flux for various micropillar structure geometries (height, pitch and diameter) in the length scale range of 1-100 μm with water as the working fluid was predicted and the optimal geometries to maximize the dry-out heat flux are suggested ($d/h \sim 0.4$-0.6 and $l/d \sim 3$). The dry-out heat flux $q_{dry\text{-}out}$ is very sensitive to the wicking length L and is governed by $q_{dry\text{-}out} \sim L^{-2}$. This suggests opportunities to enhance $q_{dry\text{-}out}$ by incorporating multiple reservoir channels inside the wicking area to reduce L. This work can be extended to other micropillar geometries such as squares but the non-uniformity of the contact angle around a pillar can result in a partial receding and partial pinning state, which needs further consideration. This work provides an important understanding of the heat transfer limitations of capillary-pumped thin-film evaporation on surfaces, and serves as a guideline for the design of high performance thermal management systems.

Chapter 3

Surface Structure Enhanced Micro-channel Flow Boiling

In this chapter, we investigate the role of surface microstructures in two-phase microchannels on long-timescale flow instabilities and CHF. We choose cylindrical micropillar arrays that optimize capillary wicking based on the model developed in Chapter 2. The aim of this chapter is to identify whether capillary flow plays an important role in flow boiling and provide insight towards methods to enhance the heat transfer performance via incorporating surface structures.

3.1 Background

The increasing power densities in various electronic devices including concentrated photovoltaics, power electronics and laser diodes pose significant thermal management challenges for the electronics industry [24,46,47]. Two-phase microchannel heat sinks are attractive to cool advanced electronic devices because they harness the latent heat of vaporization to dissipate high heat fluxes in a compact form factor. However, minimizing flow instabilities during boiling while enhancing the critical heat flux (CHF) to maximize heat dissipation has been difficult to achieve [48–50]. These flow instabilities which can be triggered by several mechanisms including explosive bubble expansion [51], upstream compressibility [52,53] and density wave oscillation [54] can lead to large pressure drop fluctuations across the channels and temperature spikes associated with liquid dry-out. This dry-out severely limits the heat removal ability of these microchannel heat sinks and leads to device failure once reaching CHF [55].

To suppress flow instability and to enhance heat transfer, recent studies have focused on incorporating various structures in microchannels, such as inlet restrictors

[27,56,57], artificial nucleation sites [27,58], vapor venting membranes [59–61], micro pin fins [62–64], and nanowire-coated surfaces [20–22] integrated into the microchannel. However, there are challenges with several of these approaches. Inlet restrictors can significantly reduce backflow but with a pressure drop penalty for the stabilization [57]. Fabricated nucleation sites have demonstrated enhanced nucleate boiling heat transfer, however, the introduction of the cavities alone can increase the instabilities [27]. Vapor venting membranes can reduce dry-out and pressure drop oscillations by locally removing the expanding vapor, however the operational range is limited due to the risk of membrane flooding at high pressures [60].

Micro and nanostructure-coated surfaces are attractive owing to the ability to modify surface wettability, generate capillarity and create nucleation sites. In fact, in pool boiling, superhydrophilic micro and nanostructures have demonstrated significantly increased CHF [42,65–70] and biphilic patterned surfaces have shown large enhancements in heat transfer coefficients [71,72]. In flow boiling, silicon nanowire-coated channel surfaces have been reported to reduce temperature fluctuations [20], increase the heat transfer coefficient and CHF, and decrease the pressure drop across the microchannels with water as the working fluid [21,22]. The enhancement mechanism was mainly attributed to both increased wettability in delaying CHF and nucleation sites formed by the nanowire bundles to improve the heat transfer coefficient in the nucleate boiling regime. At high heat fluxes, however, the annular flow regime typically dominates, where film evaporation is the important heat transfer mode [48]. Thus the role of the surface structures on the stability of the annular liquid film and on the film evaporation performance needs to be investigated. In addition, while introducing structures on the channel wall offers capillary driven liquid flow, the associated viscous resistance [73–75] from the structures, especially in the presence of shear from the vapor, can be significant. These effects are sensitive to the geometry of the structures. Therefore the precise role of the surface structures on flow boiling needs to be studied in more detail.

In this chapter, we investigated well-defined superhydrophilic microstructured surfaces in microchannels for flow boiling heat transfer. These surface structures have length scales much smaller than the height of the microchannel, and thus are different from micro pin fins that extend to the ceiling of the microchannel [62–64]. We fabricated and

characterized microchannels with well-defined micropillar arrays on the bottom channel wall, where heat was applied. The hydrophilic micropillars were only integrated on the heated bottom surface to promote wicking and film evaporation while suppressing dry-out. The sidewalls, with tailored roughness of 1-2 μm, promoted nucleation near the bottom corners [76]. Spatially decoupling nucleation to the sidewalls and film evaporation to the bottom surface promises to achieve high heat fluxes while maintaining stable heat transfer performance. We characterized structured surface microchannel and benchmark smooth surface microchannel devices in a custom closed loop setup. In particular, we investigated flow instabilities through temporally resolved temperature and pressure drop measurements, and simultaneous visualization of the flow in the device. We also characterized the heat transfer performance (the heat transfer coefficient, the CHF and the pressure drop), and explained the experimental trends for the CHF enhancement with an adiabatic liquid wicking model. The insights gained from this work are a first step towards guiding the design of stable, high performance surface structure enhanced two-phase microchannel heat sinks.

3.2 Methodology

In high heat flux applications, microchannel heat sinks usually operate in the annular flow regime due to the high vapor quality associated with heat dissipation in the confined space [77]. Since evaporation can be dominant in the annular flow regime, we designed the structured surfaces to enhance and sustain stable liquid film evaporation (Figure 3-1a and b). The structures were integrated only on the bottom heated surface where the wall temperature and the heat flux are the highest, in order to suppress liquid dry-out by generating capillary flow in the presence of menisci formation (Figure 3-1c). This capillary flow can be created both along the channel direction and from the sidewalls to the center (the dotted line regions in Figure 3-1a and 1b). The sidewalls have tailored roughness of 1-2 μm to promote nucleation [76]. By nucleating on the side walls, it is less likely to have dry-out occur on the bottom surface, which typically occurs in the case of smooth microchannel walls, owing to explosive bubble growth from it.

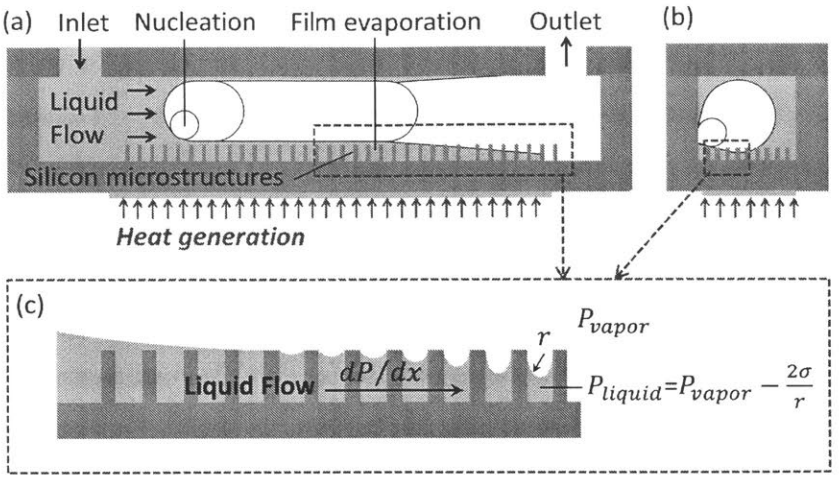

Figure 3-1 Schematic of the microchannel heat sink design with micropillars on the heated surface. (a) Side view, (b) cross-section view, and (c) magnified view of the liquid film forming menisci which create the capillary pressure gradient, *dP/dx*, that helps drive the liquid flow. The equation that describes the liquid pressure below the meniscus is the Young-Laplace equation where σ is the surface tension of the liquid, r is the radius of curvature of the local meniscus, and P_{liquid} and P_{vapor} are the local pressure of the liquid and vapor respectively.

3.2.1 Device Design and Fabrication

We investigated single microchannels with typical characteristic dimensions of 10 mm in length, 500 μm in width, and 500 μm in height. We varied the micropillar geometries on the bottom surface of the microchannel with diameters of 5-10 μm, pitches of 10-40 μm, and constant heights of 25 μm. These micropillar geometries were chosen for the following reasons: (1) The micropillars are easy to fabricate in silicon (Si) using standard etching processes and the geometries can be well-controlled in this range. (2) At these length scales, the capillary pressures that can be generated are a few kPa which are comparable to the typical microchannel pressure drop. This suggests that capillary effects are not small and can be used to manipulate flow behavior. (3) The surface structures are mechanically robust and will not change morphology (deform or form clusters) as the liquid evaporates. The specific micropillar geometries fabricated and tested are shown in Table 1, which allows investigation of the effect of micropillar diameter d and pitch l on heat transfer and flow characteristics during flow boiling. Specifically, we chose two

geometries (S3 and S4) near the optimal region based on the model developed in Chapter 2 (see Figure 2-8b) with a pillar height of 25 μm [33], and two geometries (S1 and S2) away from the optimal region.

Table 1 Geometric parameters (height, diameter and pitch) of the fabricated micropillars in the microchannel test devices.

Device No.	Height, h (μm)	Diameter, d (μm)	Pitch, l (μm)
S1	25	5	10
S2	25	5	15
S3	25	10	30
S4	25	10	40

To emulate the heat flux from a high performance electronic device, we integrated a thin-film metal heater (8.6 mm long × 380 μm wide) directly underneath the microchannel to serve as a heat source *via* Joule heating (Figure 3-1a and Figure 3-2a). In addition to the heating element, we incorporated four thin-film resistance temperature detectors (RTDs), which are commonly used for flow boiling studies [20–22,78,79], along the length of the heater to measure the microchannel backside surface temperature at different locations. Specifically, the distances x of RTD1 through RTD4 from the inlet of the microchannel were 0 mm, 1.4 mm, 5.7 mm and 10 mm respectively (Figure 3-2a).

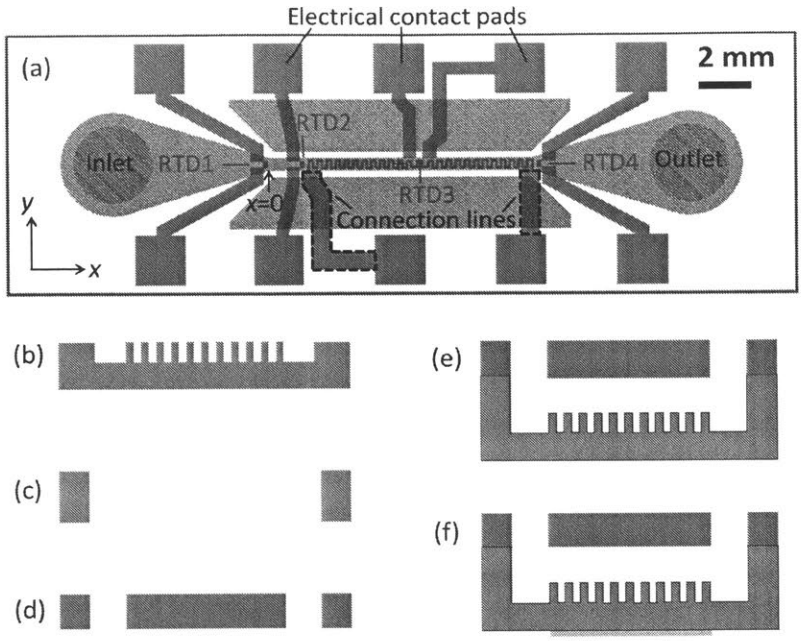

Figure 3-2 Design and fabrication process of the microchannel device. (a) Schematic (to scale) of the heater and RTDs on the backside of the microchannel device. The dotted sections are the electrical connection lines to the contact pads. (b) Micropillars of 25 μm height were etched in Si using deep reactive ion etching (DRIE). (c) A Si wafer was etched through using DRIE to define the channel. (d) Inlet and outlet ports were laser-drilled on a Pyrex glass wafer. (e) The Si layers were bonded using direct Si-Si bonding. A silicon dioxide (SiO_2) layer was thermally grown on the Si surface. The Pyrex layer was bonded to the top Si layer using anodic bonding. (f) A platinum (Pt) layer was deposited on the backside of the microchannel using electron-beam evaporation and patterned to form the heater and RTDs.

Standard silicon MEMS fabrication processes were used to create the microchannel test devices and are summarized in Figure 3-2. The micropillars were etched in a 500 μm thick Si wafer using deep reactive ion etching (DRIE) of the channel bottom surface (Figure 3-2b). A second 500 μm thick Si wafer was etched through using DRIE to define the channel sidewalls (Figure 3-2c). Inlet and outlet ports were created on a Pyrex wafer by laser drilling (Figure 3-2d). The two Si wafers were bonded together using direct Si-Si fusion bonding. A 1 μm silicon dioxide (SiO_2) layer was thermally grown on the Si surface as a hydrophilic coating on the channel walls and as an electrical insulation layer on the backside. The Pyrex wafer was subsequently bonded onto the Si wafers using anodic bonding to cover the microchannel and facilitate flow visualizations

(Figure 3-2e). Finally, a layer of ~170 nm thick platinum (Pt) was deposited on the backside of the microchannel with electron-beam evaporation and patterned by lift-off technique to serve as the heater and RTDs (Figure 3-2f). To maximize the power dissipation capability of the heater, the target heater resistance was determined by the maximum allowable heater voltage (180 V) and current (0.5 A) to prevent burnout. To achieve this target resistance of 360 Ω, we designed the thin film heater thickness and dimensions. In addition to the microstructured microchannels, we also fabricated microchannels with smooth surfaces following a similar procedure, however a polished Si wafer (roughness < 50 nm) was used instead of the micropillar wafer in the initial step (Figure 3-2b).

Figure 3-3a and b show the front and backside of a fabricated microchannel device. The two open chambers next to the microchannel (Figure 3-3a and d) were incorporated to minimize heat loss *via* conduction and to better isolate the effect of flow boiling in the microchannel. Figure 3-3c shows a magnified view of the Pt heater and an RTD on the backside of the microchannel. Figure 3-3d shows a scanning electron micrograph (SEM) of the cross-section of the microchannel (A-A plane in Figure 3-3a) with representative micropillars. The magnified views of micropillars on the channel bottom surface and a side wall near the bottom corner are shown in the left and right inset of Figure 3-3d. The side walls have small roughness (~1-2 μm) from the DRIE process (Figure 3-2c).

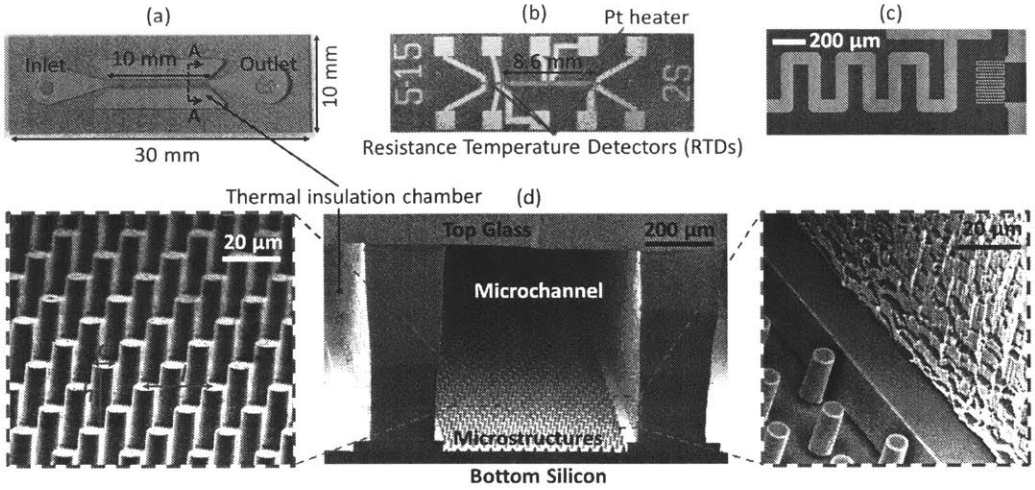

Figure 3-3 Images of a representative fabricated microchannel with micropillar arrays. Optical images of the (a) front and (b) backside of a device. (c) Optical microscope image of the heater and RTD4 on the backside of the microchannel. (d) SEM image of the cross section, A-A plane in (a), of a microchannel with magnified view of the micropillars (left inset) and a sidewall at the bottom corner (right inset).

3.2.2 Experiment Methodology and Measurement Uncertainty

We developed a closed loop test rig to characterize the microchannel test devices during flow boiling (Figure 3-4). The loop consists of a liquid reservoir, a pump to provide a constant flow rate, a valve for flow stabilization, pre-heaters to minimize subcooling, a test fixture to interface with the test device, and various sensors. Degassed and high purity water (WX0004-1, OmniSolv) was used as the working fluid. Throughout the experiment, water in the liquid reservoir was heated and degassed to saturated conditions under atmospheric pressure ($T_{water,res}$ = 100 °C for $P_{water,res}$ = 1 atm). The fluid from the reservoir was pumped through the loop using a peristaltic pump (7528-30, Cole Parmer MasterFlex L/S) to avoid contamination of the working fluid. In order to measure the flow rate with a liquid flow meter (L-50CCM-D, Alicat Scientific) which has a maximum working temperature of 60 °C, the degassed liquid was cooled *via* heat exchange with the ambient to below 60 °C as it passed through the metal tubing (the orange line in Figure 3-4 between the liquid reservoir and the flow meter). The mass flux chosen in this study was G = 300 kg/m^{2}s, which is a commonly used value in the literature [48,58–60]. In addition, this moderate mass flux allowed for high heat flux dissipation at reasonable pressure drops and pumping powers. To achieve this mass flux,

the flow rate was maintained at 4.5 ml/min. We reduced the flow rate fluctuations intrinsic to the peristaltic pump by using a high pump speed (~70 rpm) with the smallest pump tubing available (tube ID = 0.8 mm, L/S 13, Masterflex) for the pump used in the study. However, flow rate fluctuations (± 0.6 ml/min) were inevitable with the peristaltic pump at these low mass fluxes. Accordingly, a metering valve (SS-SS4-VH, Swagelok) was used to create additional hydraulic resistance (~8 kPa) for flow stabilization within the loop, and was kept at a fixed opening for all the testing (the structured surface test samples and the smooth surface test sample). Since the liquid was subcooled due to heat loss to the ambient before the microchannel test section, we added pre-heaters (FGR-030, OMEGALUX) to compensate for this heat loss. The pre-heaters maintained a minimum liquid subcooling (10 °C) while also avoiding boiling at the entrance of the test fixture. Thermocouples (K type, Omega) and pressure transducers (PX319-030A5V, Omega) were used to monitor the loop conditions. The microchannel test devices were placed in an Ultem test fixture that interfaces with the loop. The test fixture was placed in an inverted microscope (TE2000-U, Nikon) and the flow was captured using a high speed camera (Phantom v7.1, Vision Research) at 2000 frames/s. The two-phase flow pressure at the outlet of the microchannel was approximately P_{out} = 1 atm since it was connected to the liquid reservoir at atmospheric pressure.

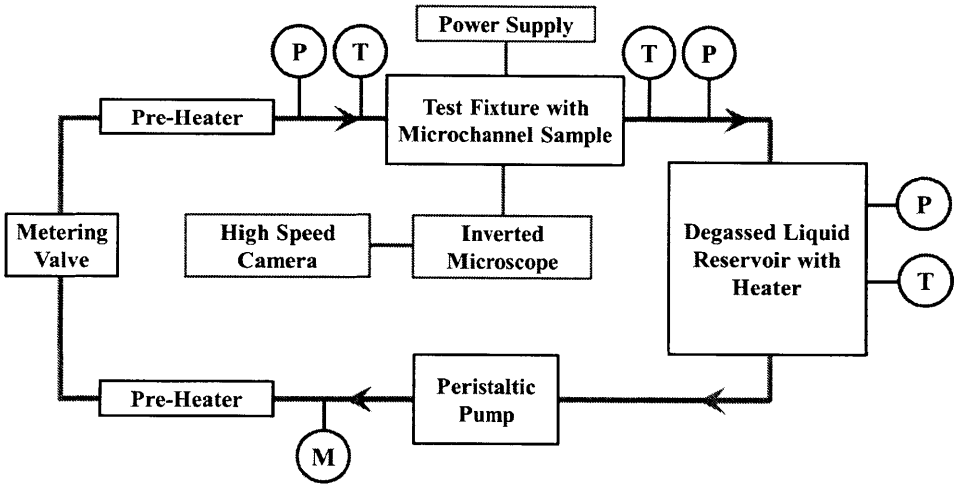

Figure 3-4 Schematic of the custom flow boiling loop used in the study. The loop consists of a liquid reservoir, a pump to provide a constant flow rate, a valve for flow stabilization, pre-heaters to minimize subcooling, a test fixture to interface with the test device, and various sensors. The components "P", "T" and "M" indicate

locations of pressure transducers, thermocouples and the liquid flow meter respectively.

Before the experiment, the Pt heater and RTDs were annealed at 400 °C for 1 hour to avoid resistance drift. The resistance R of the heater and RTDs after annealing was approximately 275 Ω at room temperature and 340 Ω at 120 °C. All the RTDs were calibrated in an oven and a linear correlation between the resistance and temperature was observed. The average sensitivity of the temperature with the resistance of the fabricated RTDs is $\Delta T = 1.4\Delta R$. The uncertainty of the resistance measurement (~1.4 Ω) resulted in an uncertainty of ±2 °C in the measured temperature. The microchannels were rinsed in acetone, isopropyl alcohol (IPA) and de-ionized water, and subsequently plasma cleaned in an oxygen environment (29 W at 500 mTorr for 15 minutes) to remove surface contamination. During the experiments, we heated the microchannel by applying a DC voltage across the thin-film heater. The microchannel heater was connected to a DC power supply (KLP 600-4-1200, Kepco), which was controlled using a PID algorithm in LabVIEW to maintain a constant output power. At each constant heat flux at steady state, the temperatures T_1 to T_4 measured by RTD1 to RTD4 respectively, the pressures and temperatures at the inlet and outlet of the microchannel, the flow rate, and the voltage and current across the heater were recorded for two minutes. The heat flux was then increased by an increment of approximately 20 W/cm^2 to the next value. Based on our measured temperature and pressure drop, the rise time to reach the next steady state was less than one minute due to the small thermal mass of the test device and the small temperature rise (~1-2 °C, see Figure 3-5). In addition, we examined the measured steady state temperature for ~5 min and no further rise was observed. Therefore the loop was left running for at least one minute to reach steady state before we acquired the data at this new heat flux.

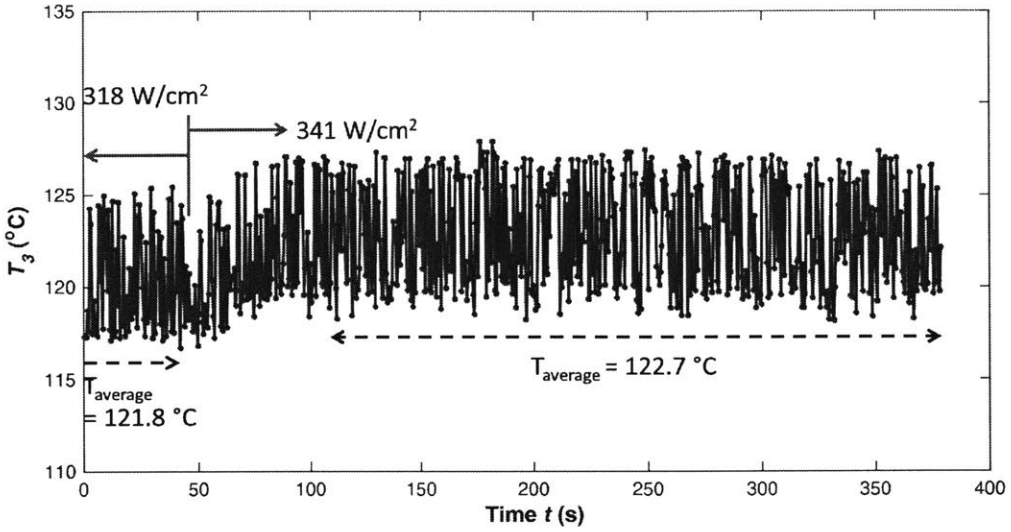

Figure 3-5 Mid-point microchannel backside temperature T_3 for sample S2. At t=45 s the heat flux was increased to 341 W/cm^2..

All the data was recorded using a data acquisition card (NI-PCI-6289, National Instruments) at a sample rate of 2 Hz. Due to the noise associated with temperature measurement (shown in Figure 3-5), we did not use higher sample rate for this study. In the next chapter we improved the setup to reduce the noise and increased the data acquisition rate to capture faster flow oscillations. For data reported in this chapter, the experiments were performed twice for each sample under the same experimental conditions to verify repeatability (the samples were cleaned using the methods described here prior to each experiment). The experimental results were similar (within the error bars) and the data reported in this manuscript are from the repeated experiment. Since the microchannel is a three-layer stack that is bonded together, we cannot remove the cover layer (without damaging the sample) of the microchannel to measure the contact angle on the channel walls. However, wicking was observed with the structured surface microchannels before and after the experiment, which suggests an apparent contact angle of 0°.

The error bars in the experiments were estimated based on the uncertainty of the measurement from the instrument error ($error_{instrument}$) and the standard deviation (STD) of multiple data points for the time-averaged data, described by equation (3.1).

$$error = \sqrt{error_{instrument}^{\ 2} + STD^2} \tag{3.1}$$

The instrument error included the resolution of the pressure transducers (±300 Pa), the data acquisition card (±1 mV) which resulted in the uncertainty of the temperature measured by the RTDs (±2 °C), the power supply (0.06 V and 0.4 mA), and the flow meter (±1 ml/min).

3.2.3 Data Processing

Since the backside temperature (T_1 to T_4) varies along the microchannel, we compared different samples using the temperature values measured at the mid-point of the microchannel backside surface by RTD3 (T_3), where the highest heater surface temperatures were observed. The outlet temperature was lower than the center as expected due to heat spreading in the substrate. The temperature rise ΔT, obtained from the difference between the mid-point temperature and the saturation temperature of the fluid (T_{sat}) at this location, is

$$\Delta T = T_3 - T_{sat} \tag{3.2}$$

The fluid pressure and the corresponding saturation temperature (approximately 100 °C) also vary along the channel. The saturation pressure (P_{sat}) of the fluid at the mid-point location was determined as the average of the measured absolute pressure values at the inlet and outlet of the microchannel,

$$P_{sat} = \frac{1}{2}(P_{in} + P_{out}) \tag{3.3}$$

The mid-point saturation temperature was then obtained from the NIST database [80] using the calculated mid-point pressure P_{sat} (equation (3.3)). The heat flux was obtained from the input electrical power (DC voltage and current), the surface area of the channel bottom wall and accounting for the loss to the environment as,

$$q'' = \frac{0.95UI - P_{loss}}{A_{mc}} \tag{3.4}$$

where U is the input voltage, I is the input current, P_{loss} is the calibrated loss to the environment (see Figure 3-6), A_{mc} is the microchannel bottom wall surface area (500 μm × 10 mm). The heat generated in the electrical connection lines to the contact pads

(enclosed in the dotted line in Figure 3-2a) was 5% of the total heat from the power supply. The factor of 0.95 (5% loss) in equation (3.4) was obtained based on the geometry of this resistance relative to the total resistance using,

$$\frac{R_c}{R_{total}} = \frac{\frac{L_c}{W_c}}{\frac{L_c}{W_c} + \frac{L_{heater}}{W_{heater}}} = 0.05 \tag{3.5}$$

where R_c and R_{total} are the resistance of the connection lines and the total heater resistance, respectively, L_c, L_{heater}, W_c and W_{heater} are the length and width of the connection lines and the heater respectively. The temperature (at the heater surface) dependent heat loss to the environment P_{loss} measured by the RTDs was obtained from experiments where the test device in the fixture was heated with the flow loop evacuated (*i.e.*, no working fluid, see Figure 3-6). A 2nd order polynomial (close to linear) fit (R^2 = 1) between P_{loss} (W) and the average microchannel backside surface temperature T_{ave} (°C) was determined from the experimental data (Figure 3-6b) as,

$$P_{loss} = 4.5\times10^{-5}T_{ave}^{\ 2} + 0.0163T_{ave} - 0.299 \tag{3.6}$$

Since T_2, T_3 and T_4 are the backside surface temperatures at the inlet, mid-point and outlet of the microchannel respectively, if we approximate the first half of the microchannel backside surface temperature as $0.5(T_2+T_3)$, and the second half as $0.5(T_3+T_4)$, the average microchannel backside surface temperature can be approximated as,

$$T_{ave} = 0.25T_2 + 0.5T_3 + 0.25T_4 \tag{3.7}$$

The overall heat transfer coefficient (HTC) which includes boiling, evaporation and conduction through the bottom Si layer was calculated from the heat flux q'' and the time-averaged temperature rise ΔT as,

$$HTC = q''/\Delta T \tag{3.8}$$

Due to the unstable nature of flow boiling, the time-averaged ΔT typically does not capture the dynamic behavior, such as periodic dry-out, which can also cause severe

transient overheating issues. Therefore we defined CHF as the heat flux beyond which the following criteria hold: (1) There is at least a 5 °C jump in ΔT; (2) There is constant or periodic dry-out in terms of time-resolved temperature and pressure drop measurements, and visualizations. In the case of periodic dry-out, the temperature fluctuations were larger than 20 °C, the pressure drop fluctuations were larger than 2 kPa, and the duration of dry-out was longer than half the cycle time.

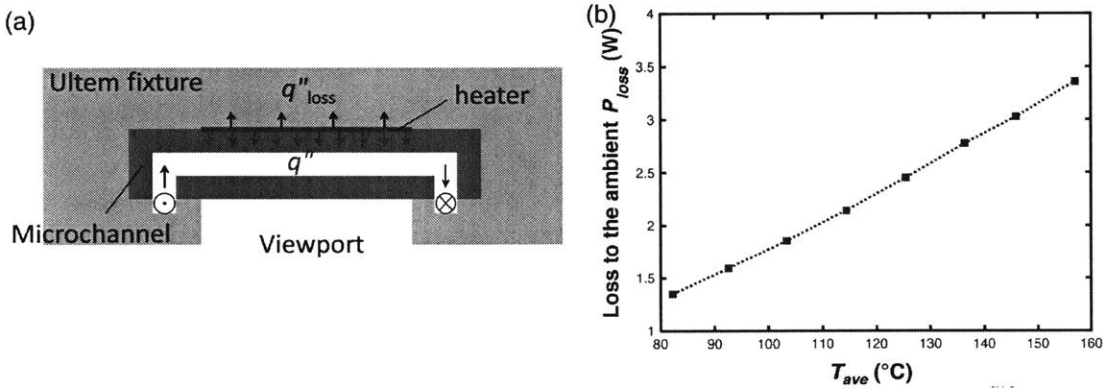

Figure 3-6 (a) Schematic of heat flux dissipated by the microchannel during flow boiling, and heat loss to the environment. (b) The calibrated heat loss as a function of average microchannel backside surface temperature T_{ave} (°C).

3.3 Results and Discussion

In this section, we first compare the stability of the measured temperature and pressure drop, and discuss the difference between the structured surface devices and the smooth surface device. Images and videos of the bottom heated surface were used to investigate the role of surface structures in annular flow stability. We then characterized the boiling curve and pressure drop curve, and discuss the heat transfer enhancement mechanism in the critical heat flux and heat transfer coefficient. Finally, we explain the different behavior among the structured surface microchannels using the liquid wicking model developed in the previous chapter and provide insights into the optimization of the micropillar geometries.

3.3.1 Long Timescale Temperature and Pressure Drop Fluctuations

Typically with smooth surface microchannels, flow instability can cause temperature and pressure drop fluctuations due to the change of flow pattern and dry-out [81,82]. To study the effect of surface structures on flow instabilities, we measured the temporal change in the backside surface temperature and pressure drop across the microchannels with structured surfaces and compared to the fluctuations of a smooth surface microchannel. Because the sampling rate is 2 Hz, we only analyze long timescale flow oscillations (~a few seconds) in this chapter. The mid-point backside surface temperature T_3 measured from RTD3 which was the highest temperature obtained compared to T_1, T_2 and T_4 was studied for this purpose.

The smooth surface and the structured surface microchannels showed similar and small fluctuations at low heat fluxes ($q'' < 400$ W/cm^2) for the mass flux investigated (G = 300 kg/m^{2}s), since the vapor quality was relatively low and long period of dry-out (>1 s) was less likely to occur compared to that at higher heat fluxes. As the heat flux increased to q'' = 430 W/cm^2, temperature spikes and increased pressure drop fluctuations were observed for the smooth surface microchannels (Figure 3-7a). At the same heat flux, all the structured surface microchannels showed small temperature (±5 °C, comparable to the noise level) and pressure drop fluctuations (±300 Pa), and the data of one representative structured surface device (S4) is shown in Figure 3-7a.

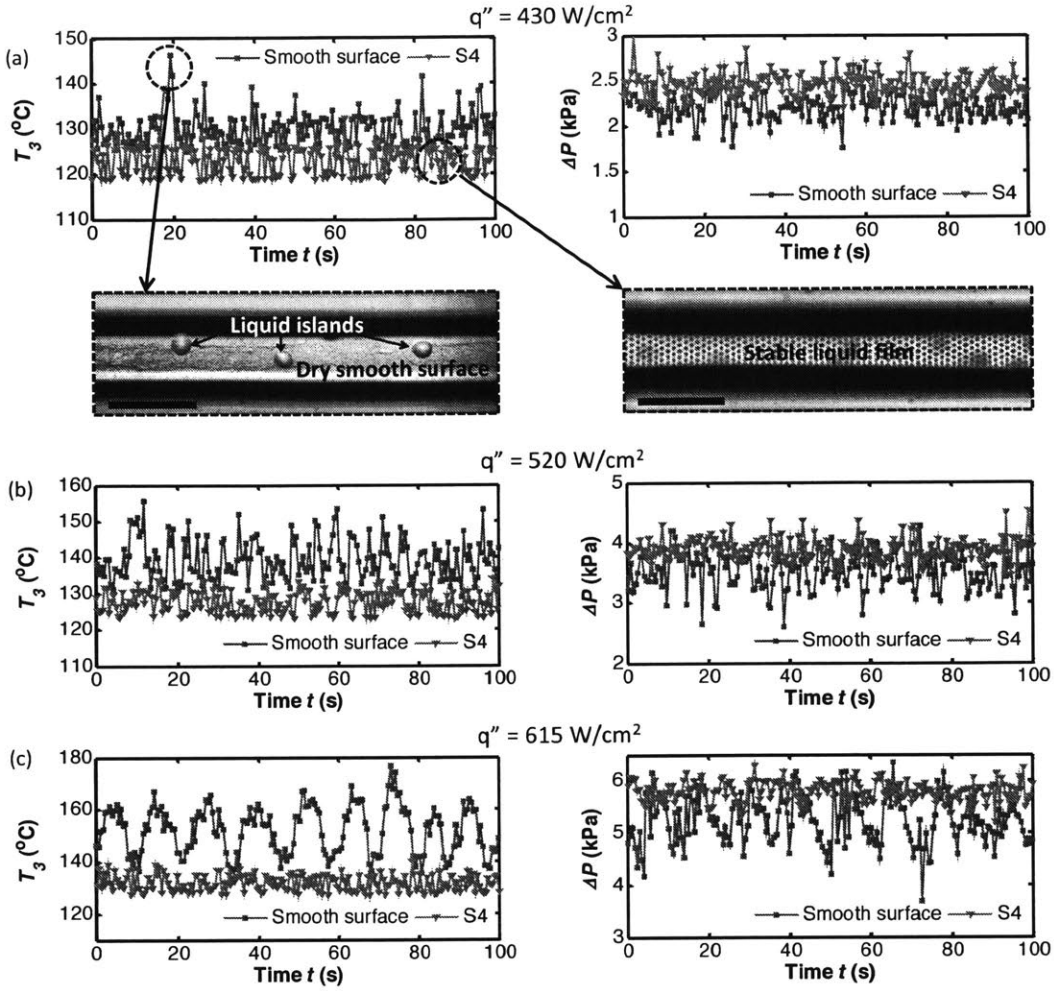

Figure 3-7 Temporally resolved temperature and pressure drop, and flow visualization at G = 300 kg/m²s. (a) Mid-point backside surface temperature T_3 and pressure drop across a smooth surface microchannel and a structured surface microchannel S4 at q'' = 430 W/cm². Insets are optical images of a smooth bottom channel surface and a structured bottom channel surface (S4). Mid-point backside surface temperature T_3 and pressure drop of a smooth surface microchannel and a structured surface microchannel S4 at (b) q'' = 520 W/cm² and (c) q'' = 615 W/cm². The uncertainties of the temperature and pressure drop measurement were approximately ±2 °C and ±300 Pa.

From the visualization of the flow, the temperature spikes of the smooth surface correspond to dry-out at the bottom microchannel surface. In contrast, flow visualization of the structured surface microchannel (Figure 3-7a) indicated a stable liquid film covering the microchannel bottom surface. This stable liquid film contributed to the stability of the temperature and the pressure drop significantly. Dry-out on the structured

surface occurred less frequently with shorter durations and less dry surface area compared to the smooth surface.

With further increases in heat flux, the temperature spikes observed on the smooth surface microchannel occurred more often and gradually developed to large amplitude (>20 °C) periodic dry-out (Figure 3-7b and c at q'' = 520 W/cm^2 and 615 W/cm^2 respectively). In comparison, the structured surface microchannel showed stable temperature (±5 °C) and pressure drop (±300 Pa) at the same heat flux (Figure 3-7b to c), even at CHF (±5-7 °C and ±300-600 Pa, Figure 3-8).

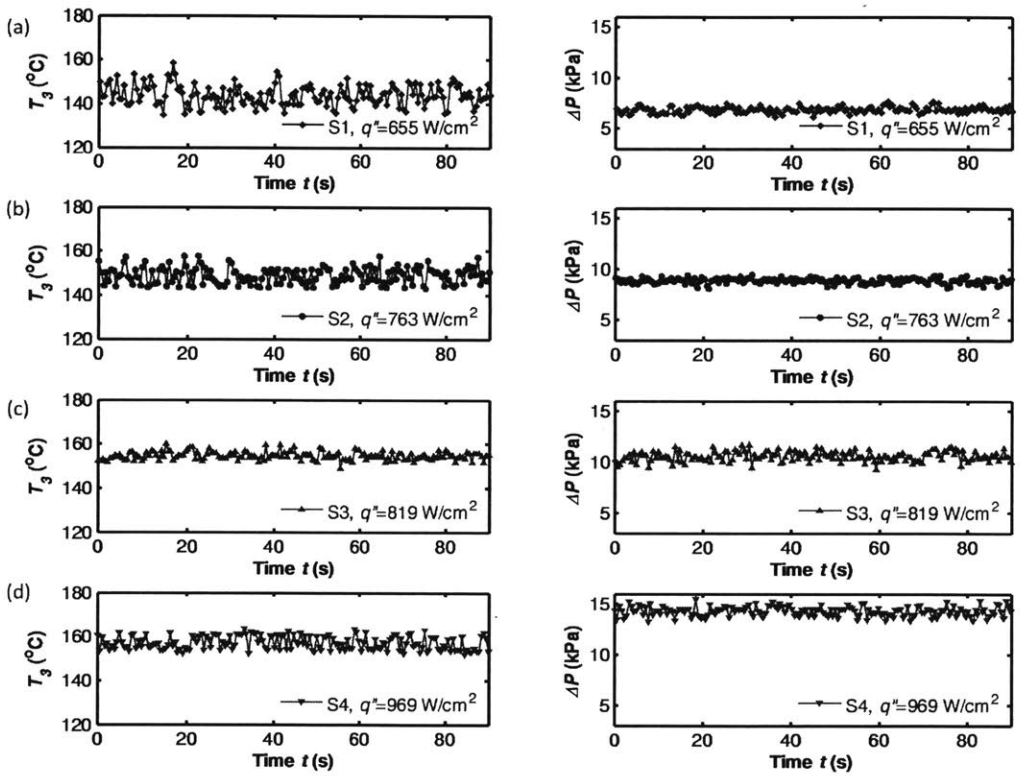

Figure 3-8 Mid-point backside surface temperature T_3 and pressure drop ΔP fluctuations of the structured surface microchannels at CHF (the highest heat flux beyond which dry-out occurred). (a) device S1 at q'' = 655 W/cm^2, (b) device S2 at q'' = 763 W/cm^2, (c) device S3 at q'' = 819 W/cm^2 and (d) device S4 at q'' = 969 W/cm^2. The mass flux G = 300 kg/m^{2}s. The uncertainties of the temperature and pressure drop measurement were approximately ±2 °C and ±300 Pa.

To further investigate the role of the structures during the dry-out process, we compared visualizations of the flow on a smooth surface and on a representative structured surface (Figure 3-9, q'' = 430 W/cm^2, G = 300 kg/m^{2}s). At t = 0 s both

microchannels were in the annular flow regime. At $t > 0$ s, the annular liquid volume started to reduce. Dry-out occurred first from the corners on the smooth surface (t = 0.002 s), and the dry surface area expanded to the center of the microchannel (0.002 s<t<0.010 s), leaving individual liquid islands. Due to the inability to supply liquid to the surface, the smooth surface could not maintain this liquid film and thus the dry-out area expanded. The smooth surface was completely dry from t = 0.012 s to 0.022 s before the liquid built up at the inlet re-flushed the channel at t = 0.024 s.

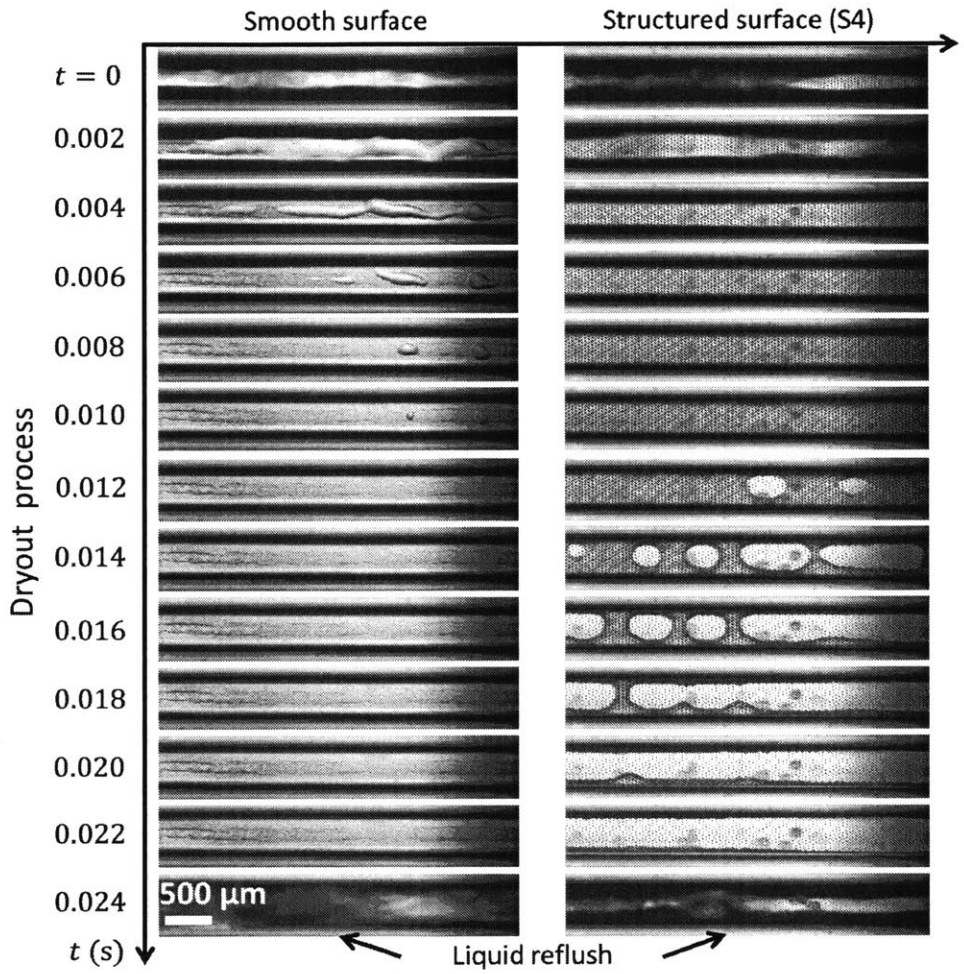

Figure 3-9 Time-lapse images of the dynamic dry-out process on a smooth surface and on a structured surface (S4) captured by a high speed camera. q'' = 430 W/cm^2 and G = 300 kg/m^{2}s. The structured surface showed less dry-out spatially and temporally compared to the smooth surface due to wicking. Dry patches formed at the center of the channel which indicated wicking in the transverse direction (from the sidewalls inward). Wicking along the channel direction also existed since the dry patches formed earlier at downstream locations of the channel.

In comparison, the structured surface (S4) maintained the liquid film due to the wicking capability of the microstructures (0.002 s<t<0.010 s), until vapor/dry islands formed first at the center instead of the sides of the channel from t=0.012 s (Figure 3-9). This suggests that there is wicking from the sides to the center where the propagation distance is the longest. This wicking sustained the liquid film (0.002 s<t<0.010 s) and delayed dry-out (t>0.012 s). In general, the wicking from the structures prevented dry-out from occurring. In addition, the dry patches formed at downstream locations before the upstream locations, which indicate that there is also wicking along the microchannel length. From the above observations, it is evident capillarity generated with the structures plays a significant role in stabilizing the liquid thin film and the resulting surface temperature.

3.3.2Heat Transfer Performance Characterization

We also characterized the time-averaged heat transfer performance of the structured surface microchannels. We compared the heat flux q'' calculated by equation (3.4) as a function of the time-averaged mid-point backside surface temperature rise ΔT (equation (3.2)) for the four microstructured surface devices (Table 1) and the smooth surface device investigated, as shown in Figure 3-10a (*i.e.*, the boiling curves). The y-axis intercept (~50 W/cm^2) at ΔT = 0 °C was mainly due to the 10 °C subcooling, which agrees well with the estimated heat flux due to subcooling $q''_{subcooling} = \dot{m}c_p\Delta T_{subcooling}/A_{mc}$ = 63 W/cm^2. The low-slope in the curves at q'' below 150 W/cm^2 was due to single phase heat transfer where the onset of nucleate boiling was indicated by the sudden drop in ΔT. After the onset of nucleate boiling, the temperature rise increased with the heat flux.

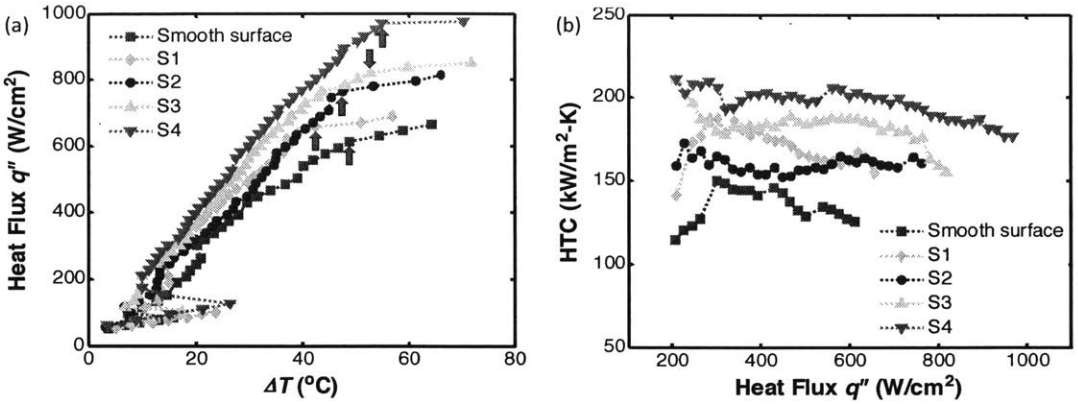

Figure 3-10 The heat transfer performance characteristics of the microchannel. (a) The boiling curve (heat flux *q"* *vs.* heater temperature rise ΔT). ΔT and *q"* were calculated by equation (3.2) and (3.4) respectively. The red arrows indicate the CHF. (b) The HTC (calculated by equation (3.8)) as a function of *q"*. The error bars for *q"* were approximately ±1%. The error bars for ΔT were approximately ±3.5 °C for the structured devices (shown for S4) and grew with the heat flux due to the increasing temperature oscillations (±3.5 °C to ±11 °C) for the smooth surface.

The red arrows in the boiling curves (Figure 3-10a) indicate the CHF. The structured surface microchannels had a clear transition at CHF, which can be seen by the sudden drop in the boiling curve slope after CHF. The time-resolved temperature and pressure drop were also very stable before and at CHF (Figure 3-8). In contrast, the smooth surface microchannel had a less obvious transition to CHF, since periodic dry-out occurred much earlier on the boiling curve from $q" = 430$ W/cm^2, as indicated by the temperature spikes (Figure 3-7). The large error bars of ΔT for the smooth surface devices at high heat fluxes were also due to the increasing temperature oscillations (Figure 3-10a). This resulted in a higher time averaged temperature rise under the same heat flux compared with the structured surface microchannels and thus a gradual decrease in the boiling curve slope. As the heat flux increased, flow instabilities (temperature spikes and pressure drop oscillations) developed to large amplitude periodic dry-out or constant dry-out (longer than one minute).

The structured surface showed an enhanced CHF with a maximum value of 969 W/cm^2 at a corresponding vapor quality χ of 0.29 achieved by device S4, which is a 57% enhancement compared with that of the smooth surface microchannel (615 W/cm^2 at $\chi = 0.19$). This CHF value is significant in comparison with similar studies in literature for a mass flux G of 300 kg/m^{2}s. The corresponding heat transfer coefficients (HTC)

which were obtained from Figure 3-10a and equation (3.8) are shown in Figure 3-10b. Note that this is the overall heat transfer coefficient (ΔT is not the wall superheat and include the temperature drop across the bottom substrate). Because T_3 which is the highest temperature measured among the four RTDs is used to conservatively represent the backside surface temperature, the HTC we report may be underestimated. The structured surface microchannels showed significantly enhanced HTC even at heat fluxes close to CHF. This is due to the fact that evaporation is dominant in the annular flow, and the structures facilitate a stable liquid film and the menisci increased the thin film area. The HTC of the structured surface devices were relatively constant, which indicates that dry-out was minimized by the structures and the thermal resistance remained relatively unchanged.

3.3.3 Pressure Drop

The hydrodynamic characteristics of the microchannels were also studied since pumping cost penalties can limit implementation of the solution in flow boiling systems [48]. Figure 3-11 shows the measured time-averaged pressure drop as a function of heat flux q''. The pressure drops across all devices were similar, which indicates that the additional pressure drop introduced by the surface structures in this study were negligible. The maximum ΔP was 14.3 kPa for device S4 at q'' = 969 W/cm^2 and G = 300 kg/m^{2}s, which resulted in a negligible pumping power of $P_{pump} = Q\Delta P$ = 1 mW, where Q is the volumetric flow rate (m^3/s). This implies that the structures did not cost more pumping power while they maintained the temperature stability and enhanced heat transfer. This result is attributed to the liquid-vapor interface only forming menisci within the structures when there is insufficient liquid supply (Figure 3-1c) which is usually at the downstream section of the microchannel. In the devices tested, there was sufficient liquid supply upstream such that the majority of liquid was on top of the structures and the structures only acted as surface roughness and did not introduce noticeable extra viscous pressure drop. In addition, wicking from the sidewalls to the center of the bottom surface did not contribute to the pressure drop along the microchannel direction.

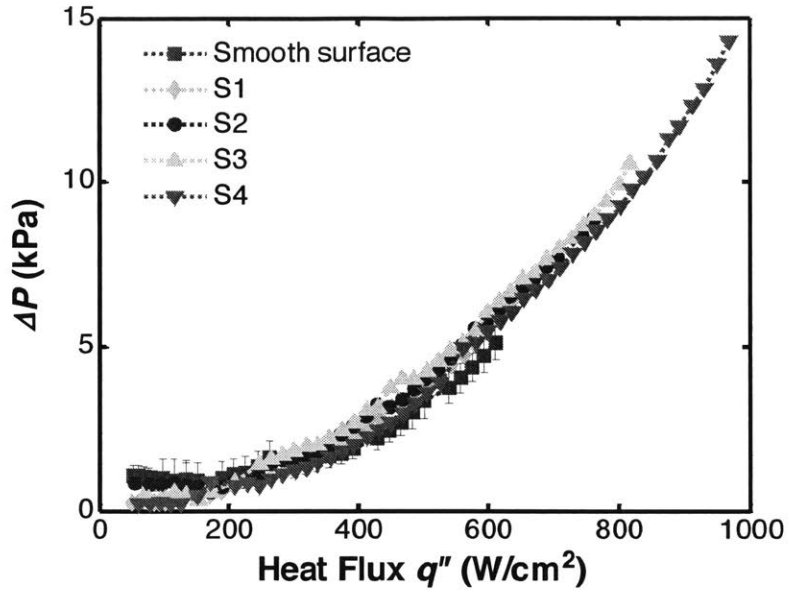

Figure 3-11 Pressure drop across the microchannel as a function of heat flux for the devices investigated. The data were plotted until CHF. Error bars in pressure were approximately ±430 Pa (shown for the smooth surface microchannel), which were calculated from the standard deviation of the temporal pressure measurement and the accuracy of the pressure transducers.

3.3.4 Mechanism of Enhancement

To further support our explanation for the role of the micropillar geometries in the wicking performance, we first compare the CHF measured in the microchannels to the transverse liquid propagation flow rate (from the side walls to the center) in the micropillar arrays (Figure 3-1c) using a simple, adiabatic (no phase-change) wicking model developed by Xiao *et al.* [33]. We then compare the CHF values with the optimization model developed in Chapter 2. Both models suggest that fluid wicking is the key mechanism for the enhancement of CHF in flow boiling.

The model by Xiao *et al.* solves the 1-D Brinkman equation to obtain the liquid velocity in porous media. The model framework gives the velocity profile,

$$u = Ae^{\alpha\sqrt{\varepsilon}y} + Be^{\alpha\sqrt{\varepsilon}y} - \frac{1}{\alpha^2\mu}\frac{dP}{dx} \tag{3.9}$$

where u is the velocity, dP/dx is the pressure gradient which drives the liquid flow, μ is the viscosity of the liquid, ε is the porosity of the micropillar arrays, and α^{-2} is the permeability that accounts for the drag introduced by porous media, A and B are constants based on the geometries of the micropillars. [33]

To estimate the driving pressure gradient dP/dx in equation (3.9) in the transverse direction of the microchannel, we assume that (1) the dry-out location has the largest meniscus curvature k (*i.e.*, minimum radius of curvature $r = 1/\kappa$) since the liquid level is the lowest. Therefore the liquid pressure is the lowest at the dry-out point based on the Young-Laplace equation ($P_{cap} = P_{vapor} - P_{liquid} = 2\sigma/r$); (2) at the dry-out location, the contact angle of water on silicon dioxide (pillar surface) is the receding contact angle θ_r ($\theta_r \approx 15°$) [43]; (3) the pressure gradient is approximated as $dP/dx = (P_{max} - P_{min})/L_w$, where P_{max} is the maximum pressure along the wicking path which is at the sidewalls ($P_{max} \approx P_{vapor}$) since the curvature is approximately zero, $P_{\min}$ is the pressure at the dry-out location ($P_{min} = P_{vapor} - 2\sigma/r$), and L_w is the wicking distance. From above, $dP/dx = P_{cap}/L_w$; (4) P_{cap} is derived using a force balance on the liquid-vapor interface, $P_{cap}(l^2 - 0.25\pi d^2) = \gamma \pi d \cos\theta_r$ [83,84]; (5) the longest wicking distance is from one sidewall to the other sidewall since dry-out can happen at random locations, so maximum $L_w = W$, where W is the width of the microchannel (W = 500 μm). With these assumptions, we calculated the average liquid wicking velocity u_{ave} which is proportional to the flow rate of the wicking liquid film,

$$u_{ave} = \frac{1}{h}\int_{y=0}^{y=h} u dy \tag{3.10}$$

where the height h is fixed (h = 25 μm). The result is shown in Figure 10, where u_{ave} is plotted as a function of l and d. The geometries of the micropillars investigated in this study are also shown in symbols in Figure 3-12 (device S1 to S4).

By comparing the results in Figure 3-12 and Figure Figure 3-10, the microstructures that led to a higher liquid wicking velocity also had a higher CHF. This positive correlation between wicking velocity and CHF is expected based on our proposed mechanism, since efficient liquid transport helped sustain the thin film evaporation and prevent dry-out. Figure 3-12 also indicates that the wicking velocity

depends both on the capillary pressure which creates the driving pressure gradient, and the viscous resistance, which hinders effective liquid propagation. Both terms depend on the structure geometry. Specifically, the capillary pressure approximately scales with $1/l$, and the viscous drag scales with $1/l^2$, thus as l decreases the drag force increases faster than the driving capillary pressure. This is the reason device S1 has lower wicking velocity even though it has higher capillary pressure (due to smaller spacing) compared to device S4, because the increased viscous resistance is more significant than the increase of the pressure gradient. In fact, the geometry of the structures can be further optimized to maximize the wicking capability, and hence enhance the flow stability and heat transfer.

While this wicking model explains the trends of the experimental results in flow boiling, the effects of evaporation and the curved interfaces were not accounted for. Thus we also compare the numerical model developed in Chapter 2 which takes these two factors into consideration, with the experimental CHF values. Interestingly, by comparing Figure 2-8b and Figure 3-10a, we found that while the trend is consistent with sample S1 and S2 which were not optimized for wicking, the model predicts that sample S3 has a higher dry-out heat flux than S4, in contrary to the experimental measurement of flow boiling CHF. One possible reason for the discrepancy could be that the effect of vapor shear present in flow boiling (*i.e.*, an axially varying vapor pressure) is not captured in the model which assumes a constant vapor pressure. Because vapor shear can help to drive the liquid flow on the channel wall, incorporating structures on the wall can potentially reduce the driving force from the vapor shear. This may explain that sample S4 with sparser micropillars performs better than S3. A more comprehensive model which accounts for wicking in both lateral and axial direction needs to be developed in the future to provide more detailed understanding of the role of surface structures on flow boiling.

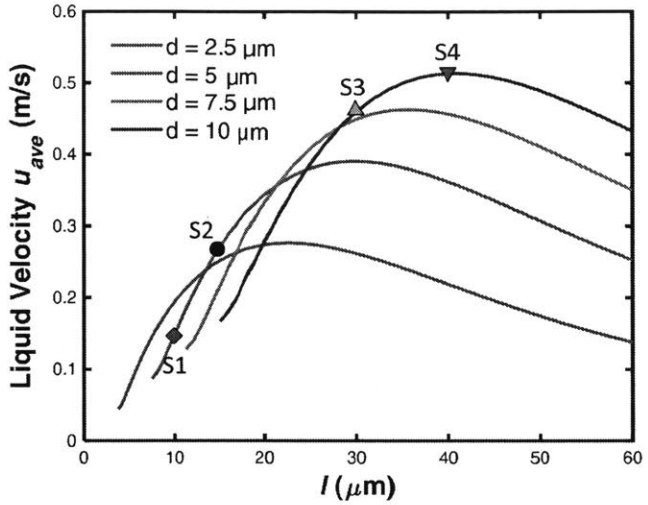

Figure 3-12 The liquid wicking velocity u_{ave} as a function of the diameters d and pitches l of the micropillars, when the height h is fixed (h = 25 μm). u_{ave} is calculated by equation (10), and the magnitude of u_{ave} is proportional to the flow rate of the wicking liquid film in the pillar arrays. The symbols on the curves mark the locations of the geometries of the micropillars investigated in this study.

In conclusion, we have demonstrated the design of a two-phase microchannel heat sink incorporated with micropillar arrays as a platform to study the effect of surface structures on flow boiling in microchannels. The design decouples thin film evaporation and nucleation by promoting capillary flow on the bottom heated surface while facilitating nucleation from the sidewalls. The structures reduced flow boiling instability significantly in the annular flow regime, and achieved very stable surface temperature and channel pressure drop even at high heat fluxes close to CHF. The smooth surface showed frequent temperature spikes and pressure drop fluctuations due to dry-out, which developed gradually to CHF. Visualization of the flow pattern and the dry-out process indicates that the micropillar surface can promote capillary flow and increase flow stability by maintaining a stable annular flow and high-performance thin film evaporation. This stabilized annular flow and thin film evaporation contributed to an enhanced HTC and CHF (maximum 57%) compared to a smooth surface microchannel. The pressure drop across all devices was similar, which indicates that the additional pressure drop introduced by the surface structures in this study was negligible. A liquid wicking model in the transverse direction of the channel was developed to explain the trend in the enhancement of CHF among the structured devices. Both the experimental

results and the model suggest that capillary pressure can be maximized without introducing large viscous resistance when the microstructure geometry is optimized. A more comprehensive model that accounts for wicking in the microchannel axial direction will be developed in the future to aid in further understanding of the role of surface structures on flow boiling. This work provides important insights into the role and promise of incorporating micropillar designs in high performance microchannel heat sinks.

Chapter 4

Role of Surface Structures on Short Timescale Instabilities

In the previous chapter we investigated long timescale flow instabilities prior to CHF conditions in two-phase microchannels. While much work has focused on long-timescale (~seconds) flow oscillations, the rapid growth of vapor bubbles which can cause flow reversal, occurs on a much shorter timescale (~tens of milliseconds). In this chapter we discuss high frequency flow instabilities in these systems and the role of surface structures. High frequency oscillation has often been visualized with high-speed imaging, but its effect on the instantaneous temperature has not been fully investigated due to the typical low sampling rates of the sensors. We investigate the temperature response as a result of the high-frequency flow oscillation in microchannels and the effect of surface microstructures on this temperature oscillation with a measurement data acquisition rate of 1000 Hz. Similarly, the result here suggests that promoting capillary wicking via surface structures is very promising to reduce high-frequency temperature oscillations in two-phase microchannel thermal management devices.

4.1 Background

A major challenge of two-phase cooling is flow instability which can cause significant temperature and pressure drop oscillations that lead to thermal and mechanical

fatigue.[12,85] A few types of flow instabilities include Ledinegg instability,[53,86] density wave oscillation[87] and pressure drop oscillation[88]. The pressure drop type oscillation occurs when the flow loop has a compressible volume upstream (e.g., a surge tank), usually much larger than the volume of the channel, and therefore is associated with a long-timescale oscillation period (1-50 second). Experimentally, long-timescale flow oscillations have been commonly observed, and they are known to lead to severe temperature and pressure drop fluctuations,[89] and often trigger premature critical heat flux (CHF).[56,82] For microchannels where the channel diameter is much smaller than the capillary length, another type of flow instability with an orders-of-magnitude shorter timescale (~tens of milliseconds) has also been observed.[21,22,51,90,91] It is usually associated with the rapid growth of vapor bubbles expanding along the channel direction in the nucleate boiling regime[51] and the fast switching between dry-out and liquid rewetting in the annular flow regime.[21,22,90] While this high-frequency oscillation has been visualized with high-speed images,[21,22,51,90,91] typical measurement sampling rates in flow boiling studies are not high enough to capture the corresponding temperature and pressure drop oscillations on this timescale. Recent transient measurement studies[79,92] have shown fast (< 20 milliseconds) and large-amplitude wall temperature changes as a vapor slug passes through the microchannel. These results suggest there is a need to further characterize the short-timescale temperature oscillations at various heat flux conditions and provide strategies to mitigate this instability.

Recent efforts to suppress flow instability mainly include inlet restrictors or valves,[27,56] pin fins,[64,93] and surface structures.[21–23,94] While inlet restrictors and pin fins are effective in reducing reverse flow, they typically introduce additional pressure drop. The use of surface micro- and nanostructures to mitigate flow boiling instability[20] and enhance the heat transfer performance[21–23,94,95] has been attractive because of their ability to modify wetting and liquid spreading behavior[16,96,97], without adding a significant flow resistance. Recently, surface structures have been incorporated into microchannels to reduce temperature oscillation by promoting an early onset of nucleate boiling[20,21], and enhance the CHF.[22,23] While the structures have been shown to reduce the long-timescale dry-out event[23], their effect on high-frequency flow oscillation has not been investigated in detail.

In this chapter, we investigated the role of surface microstructures in suppressing surface temperature oscillations during high-frequency flow instability events. Following the design and methods described in the previous chapter, we fabricated microchannels with smooth surface and microstructured surface. We improved the setup to reduce noise in temperature measurement. High-frequency temperature oscillations of the microchannels under different mass fluxes (100-300 kg/m^2s) and heat fluxes were measured with high sampling rates and the results were compared with high-speed imaging. We analyzed the frequency and the magnitude of the temperature oscillations, and discuss the effect of surface structures under low and high heat flux conditions, respectively.

4.2 Experimental Method

Microchannels (500 μm in width and height, 10 mm in length, Figure 4-1) investigated in this chapter were fabricated following the procedure described in the previous chapter. Cylindrical micropillars were etched onto the bottom surface of the channel and their geometries (diameter d=10 μm, pitch l=30 μm and height h=25 μm) were chosen to have both large permeability and capillary pressure.[98] In fact this is the optimal geometry based on our model developed in Chapter 2 (Figure 2-8b). Similarly, microstructure shapes such as pyramids or cones may also serve as effective wick geometires[31] with dimensions optimized to promote capillary flow, which can be investigated in future work. The heater and RTDs were incorporated on the backside of the microchannel to emulate the heat generation and measure the temperature of an electronic component (e.g., transistors). More details can be found in chapter 3.

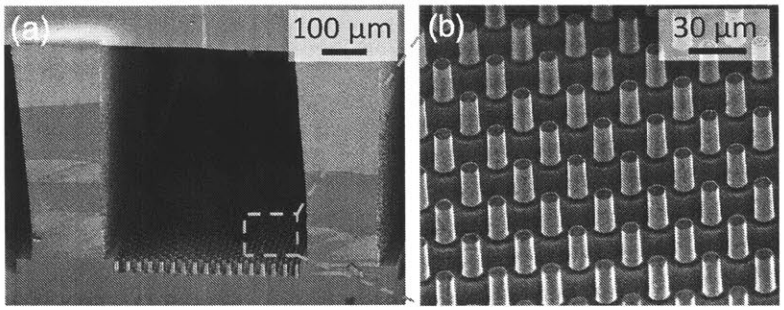

Figure 4-1 SEM of the fabricated microchannel with microstructures investigated in this study. (a) Cross-section view of the microchannel and (b) the micropillar arrays (diameter d=10 μm, pitch l=30 μm and height h=25 μm).

We tested our devices using a customized flow loop (Figure 4-2) similar to the experimental setup in the previous chapter. The main differences are that (1) The fluid tubing connecting the outlet of the microchannel and the liquid reservoir was covered with thermal insulation to minimize condensation of the two-phase flow which may impose an additional mode of instability from flow condensation; (2) A more stable power supply (N5752A, Agilent Technologies) was used. Three different flow rates (G=100, 200 and 300 kg/m^{2}s) were investigated, and degassed deionized water (100 °C at 1 atm) was used as the test fluid. The inlet subcooling was 10 °C to minimize sensible heating of the fluid while avoiding boiling upstream of the microchannel. A peristaltic pump was used to avoid contamination of the test fluid. Although the peristaltic pump intrinsically causes oscillations in the liquid mass flow rate, the frequency of the pump head (1.6-5.1 Hz) is an order of magnitude smaller than that of the flow oscillations observed in the microchannel (20-60 Hz). Therefore during a single oscillation cycle in the microchannel, the flow supplied by the pump is almost constant. Calibration of RTDs (the results are shown in Figure 4-3) and the heat flux calculation (based on the heater input power) are discussed in detail in the previous chapter. During the experiments, the heat fluxes were incremented every 10 minutes (longer than the 2 minutes in the previous chapter to include more data points), the temperature and pressure were measured with a much higher sampling rate of 1000 Hz, and high speed videos were recorded with 2000 frames per second.

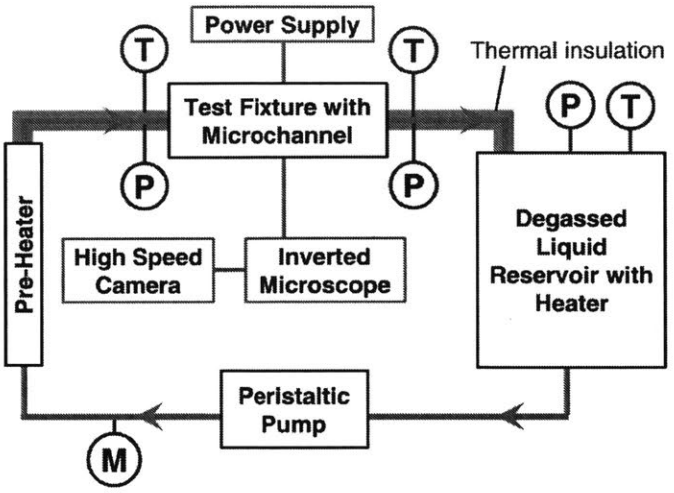

Figure 4-2 Schematic of the experimental setup. T, P and M are temperature, pressure and flow rate sensors, respectively.

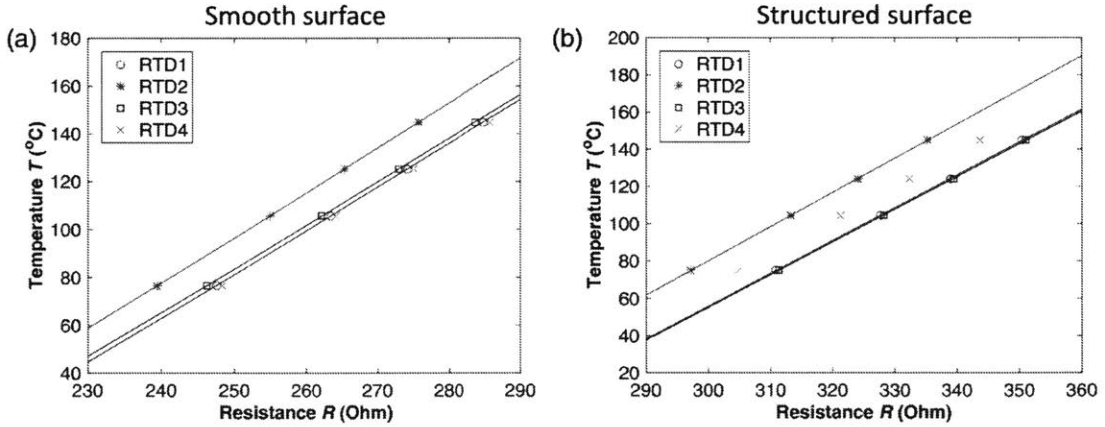

Figure 4-3 Calibration results (temperature vs. resistance) of the RTDs for (a) the smooth surface and (b) the structured surface microchannels. The symbols are the measured data and the lines are linear fits.

4.3 Results and Discussion

The heat flux q" is shown as a function of the time-averaged temperature rise ΔT at 100 kg/m^{2}s in Figure 4-4. Similarly, T_3 (measured by RTD3) which is the highest temperature measured among the RTDs was used as a conservative way of estimating the temperature rise ($\Delta T = T_3 - T_{sat}$). Note that ΔT is not the wall superheat and includes the temperature drop across the substrate silicon (500 μm thick). The experiments were

terminated when ΔT approximately approached 60 °C to prevent mechanical failure of the devices (may be caused by thermal gradient and high temperature), and the highest heat fluxes in Figure 4-4 are not CHF based on the conventional definition (i.e., no temperature excursion was observed). Although the maximum ΔT (50 °C at 500 W/cm^2) for the structured surface microchannel is high, it was achieved with a small mass flux (100 kg/m^{2}s) and can be reduced by increasing the mass flux (see Figure 3-10).[23] The experiments were repeated and similar boiling curves were observed (Figure 4-5).

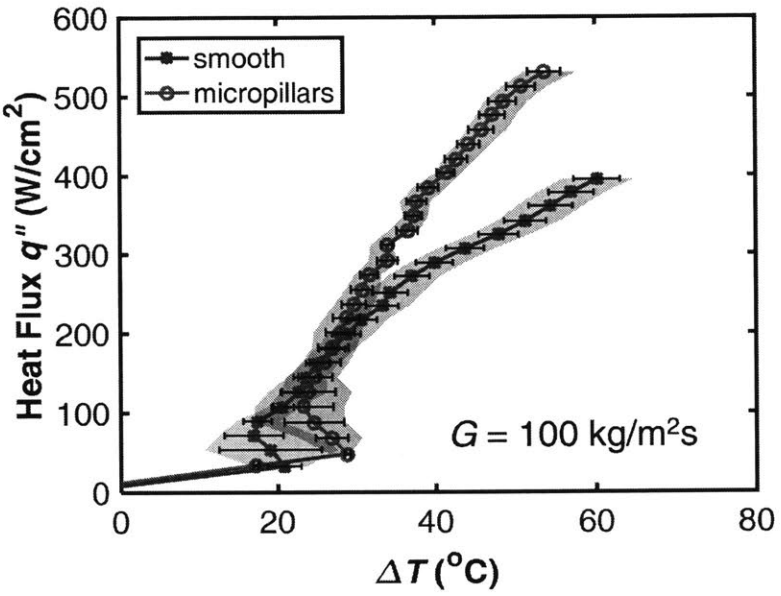

Figure 4-4 Comparison of the heat flux as a function of temperature rise (the boiling curve) of a smooth surface and a structured surface microchannel at G = 100 kg/m^{2}s. The microstructures have geometries of d=10 μm, l=30 μm, and h=25 μm. The shaded regions are the temperature rise oscillation range calculated based on the 5 to 95 percentile of the data (5% of the measured temperature is below or above the bounds), to exclude occasional outlier data. Note that the highest heat flux is not CHF.

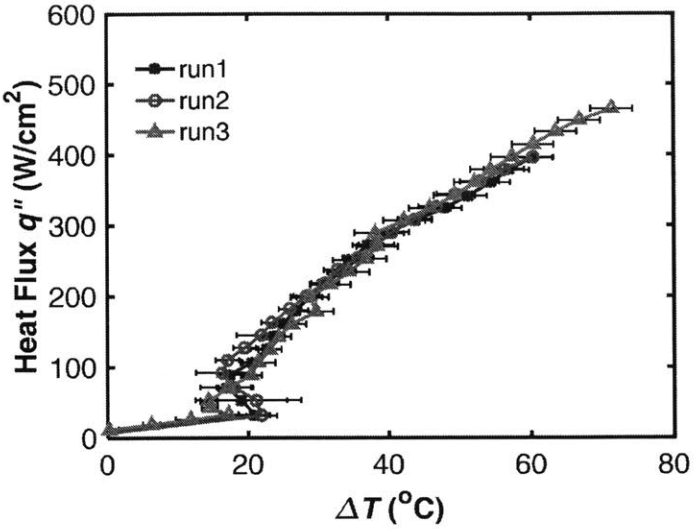

Figure 4-5 Repeated boiling curve measurements for the smooth surface microchannel at G=100 kg/m^{2}s. The highest data points are not CHF based on the conventional definition (i.e., no temperature excursion was observed).

At a low mass flux (100 kg/m^{2}s), CHF values typically reported in literature[48] for a smooth surface microchannel are lower (< 400 W/cm^2), and are associated with long-timescale temperature excursions.[81,99] We designed our loop to eliminate any components with substantial compressible volume (surge tank and condenser) which may trigger these long-timescale instabilities. This enabled us to better isolate and capture the short-timescale instability.

We also show the range of the temperature oscillation at each heat flux as the shaded regions in Figure 4-4. The lower and upper bounds were calculated based on 5th and 95th percentile of the measured temperature (1000 data points per second for at least 2 minutes at the steady state). The 95th percentile (the upper bound) is the value below which 95% of all the measured temperature falls. Similarly, the 5th percentile (the lower bound) is the value below which 5% of all the measured temperature falls. T oscillation range thus implies 90% of all the measured temperatures were between this range, to allow for some occasional. We did not use the difference between the maximum and minimum values (i.e., the 0th and 100th percentile) because it overestimates the peak-to-peak oscillation magnitude. An example of the T oscillation Range is shown in Figure 4-6 for smooth surface microchannel at G=100 kg/m^{2}s and q"=397 W/cm^2.

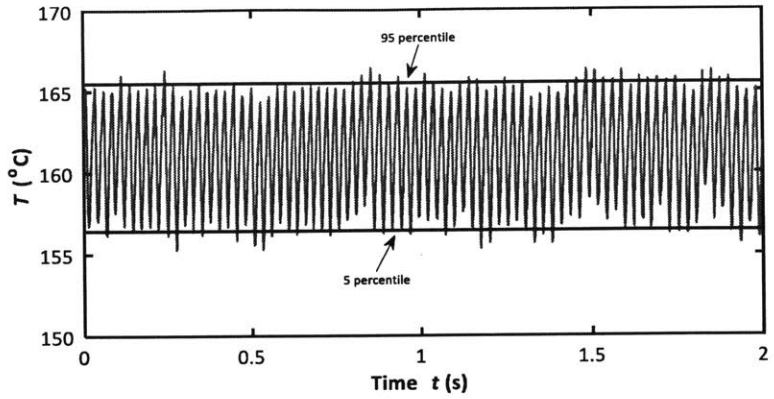

Figure 4-6 T_3 oscillation of the smooth surface microchannel at G=100 kg/m^{2}s and q"=397 W/cm^2. The blue lines are the value of the 95 percentile and 5 percentile respectively, to represent the oscillation bounds for the majority of the measured data.

In Figure 4-4, initially, single phase heat transfer at heat fluxes below 40 W/cm^2 led to curves with low slopes and the temperature oscillations were small. The onset of nucleate boiling (ONB) is indicated by the drop in ΔT due to an increase of the heat transfer coefficient. Large temperature oscillations (>10 °C) were observed following the ONB. High speed images show that the temperature oscillations at such low vapor quality were mainly caused by oscillation between single phase and two-phase flow. Specifically, the temperature decreased during bubble growth and departure (two-phase flow) and increased during the wait time (single phase flow, see Figure 4-7). As the heat flux was increased, the temperature oscillations reduced due to more frequent nucleation events. No apparent difference was observed for the smooth and structured surface samples because the bubble nucleation occurred from the sidewalls which were the same for both samples. These observations suggest that reducing flow instability at low heat flux requires promoting nucleation and this is supported by studies that incorporated dedicated/designed nucleation sites such as nanowire bundles and reentrant cavities.[20,81]

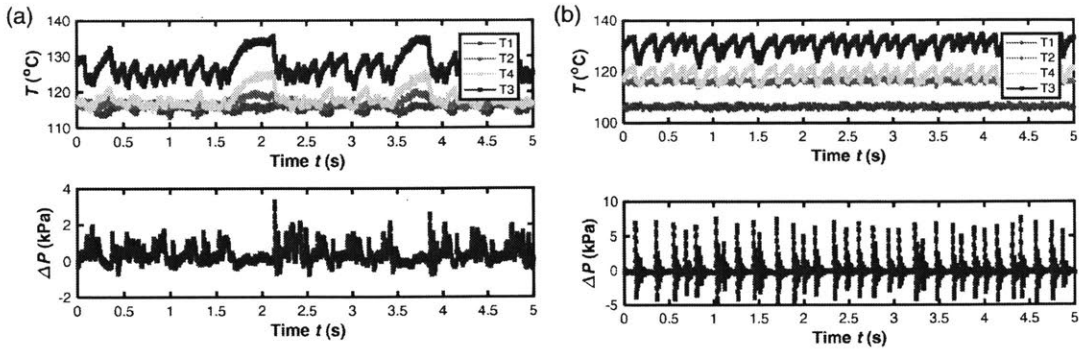

Figure 4-7 Temperature and pressure drop oscillations of the (a) smooth and (b) structured surface microchannels at low heat fluxes (G=300 kg/m^{2}s, q"=110 W/cm^2).

As the heat flux was further increased and the flow transitioned to the annular flow regime (>250 W/cm^2), temperature oscillations increased for the smooth surface microchannel and the time-averaged temperature rise also exceeded the structured surface microchannel (Figure 4-4). High speed visualizations show that the flow switched between complete dry-out and rewetting annular two-phase flow with a frequency approaching 40 Hz. This result indicates that although no CHF can be identified from the boiling curve, complete dry-out has already occurred periodically and can only be captured by temperature measurement with a high sampling rate. The time-resolved temperature at a relatively high heat flux (≈400 W/cm^2) is shown in Figure 4-8a (smooth surface) and Figure 4-8b (structured surface). The smooth surface microchannel showed fast temperature oscillations with a peak-to-peak value (magnitude) of approximately 10 °C (T_3) and a period of 26 ms. T_2 and T_4 showed a similar oscillation frequency but lower amplitudes due to heat spreading away from the heater. In comparison, the temperature of the structured surface remained relatively constant and no cyclic oscillations were observed.

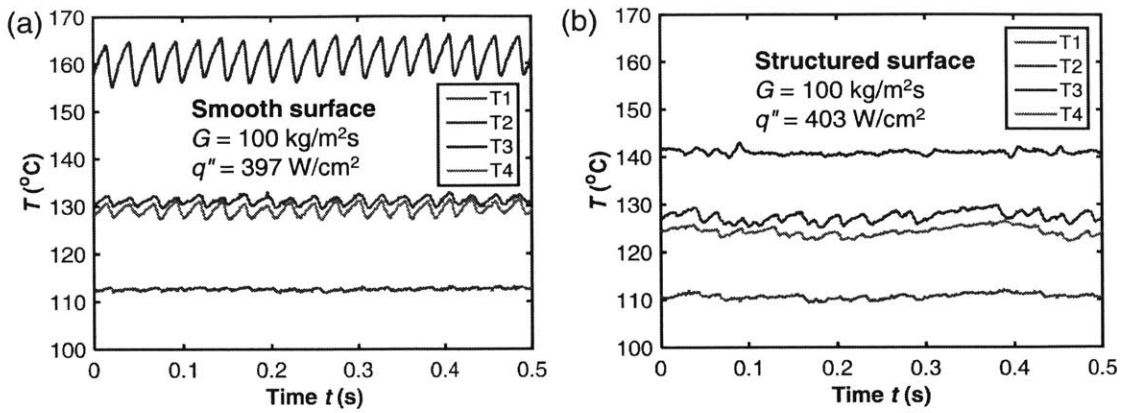

Figure 4-8 Time-resolved temperature measurement of (b) the smooth surface microchannel and (c) the structured surface microchannel at G = 100 kg/m^{2}s and a heat flux of approximately 400 W/cm^2. T_1-T_4 are the temperatures at the backside of the microchannel and are located at the inlet, before the heater, at the center of the heater, and at the outlet, respectively, based on RTD1-4.

We compared the high speed images with the measured temperatures on the backside of the microchannels. At a heat flux of ≈400 W/cm^2, time-lapse images (Figure 4-9a) show that in one cycle, the annular flow dried out on the smooth surface and remained dry for longer than half of the period of the cycle, until the rewetting flow flushed the channel. The temperature decreased during two-phase flow and increased during dry-out (single-phase vapor). For the structured surface, dry-out was significantly suppressed (Figure 4-9b), which led to a relatively stable and lower temperature. The wicking capability of the structures stabilized the temperature under the short-timescale flow oscillation. The fluctuation of the liquid thickness which can promote (liquid thickness ≤ micropillar height) or eliminate (liquid thickness > micropillar height) thin-film evaporation within the microstructures may have caused the small temperature variation of T_2 and T_4 as shown in Figure 4-8b.

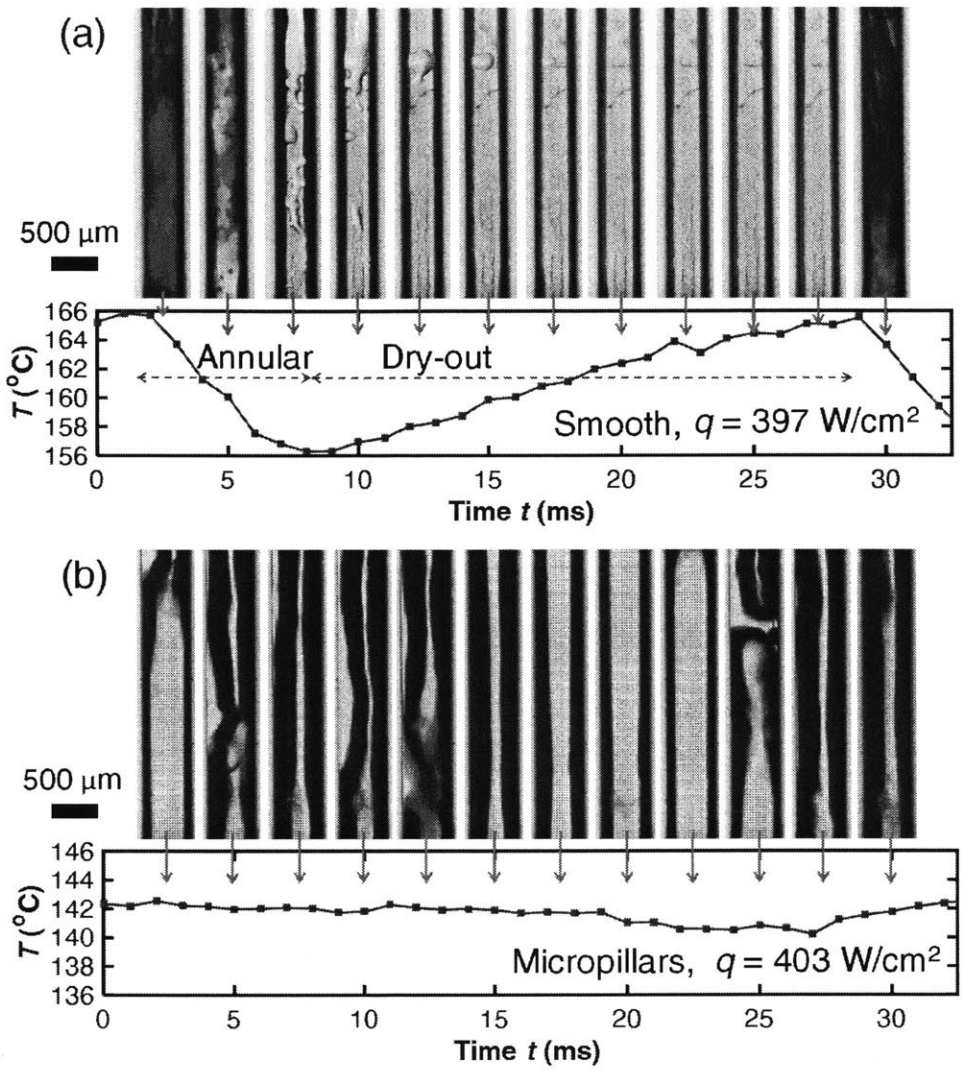

Figure 4-9 Time-lapse images of the two-phase flow and T_3 (measured by RTD3 located at the center of the heater on the backside of the microchannel) for the (a) smooth surface microchannel and (b) structured surface microchannel. The applied heat flux was ≈400 W/cm^2. The error bars for T was approximately 1 °C.

We calculated the frequency of the temperature oscillations using the fast Fourier transform (FFT) method. A Gaussian fit was used to determine the peak frequency f and the standard deviation σ, which was used as the error bars for f (see Figure 4-10 for an example). The frequency results are shown in Figure 4-11a. The frequencies corresponded to oscillation periods from 17 to 50 ms for heat fluxes higher than 150 W/cm^2. We also obtained the flow oscillation frequency from high speed images by counting the number of cycles within the duration of the video. The two frequencies

show good agreement (Figure 4-11a), indicating that the temperature oscillations reflect the flow behavior in the microchannel. The frequency increased with both the applied heat flux and the mass flux. A higher heat flux increased the rate of vapor generation, which accelerated the accumulation of the incoming liquid upstream of the microchannel. A higher mass flux resisted the flow reversal and aided the liquid rewetting process. FFT analysis of the temperature of the structured surface did not show apparent peak frequencies, because the measured temperature was not periodic and was more stable.

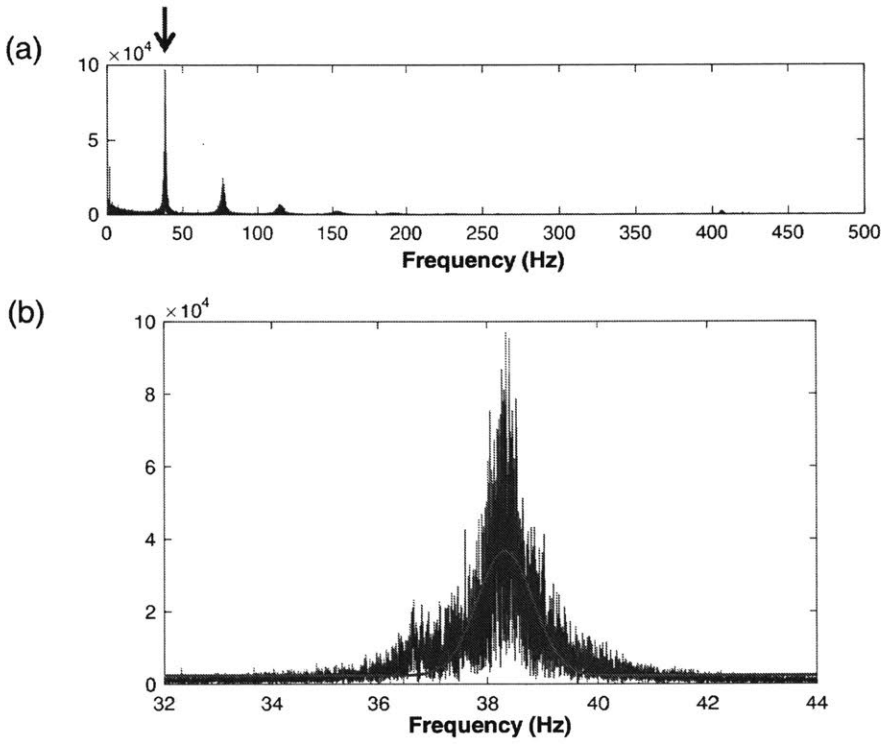

Figure 4-10 (a) The FFT of the *T* oscillation for smooth surface at $G = 100$ kg/m^{2}s, $q'' \approx 400$ W/cm^2. The peak is labeled by the red arrow. (b) A Gaussian fit was used to determine the peak frequency (the center frequency of the peak) and the standard deviation.

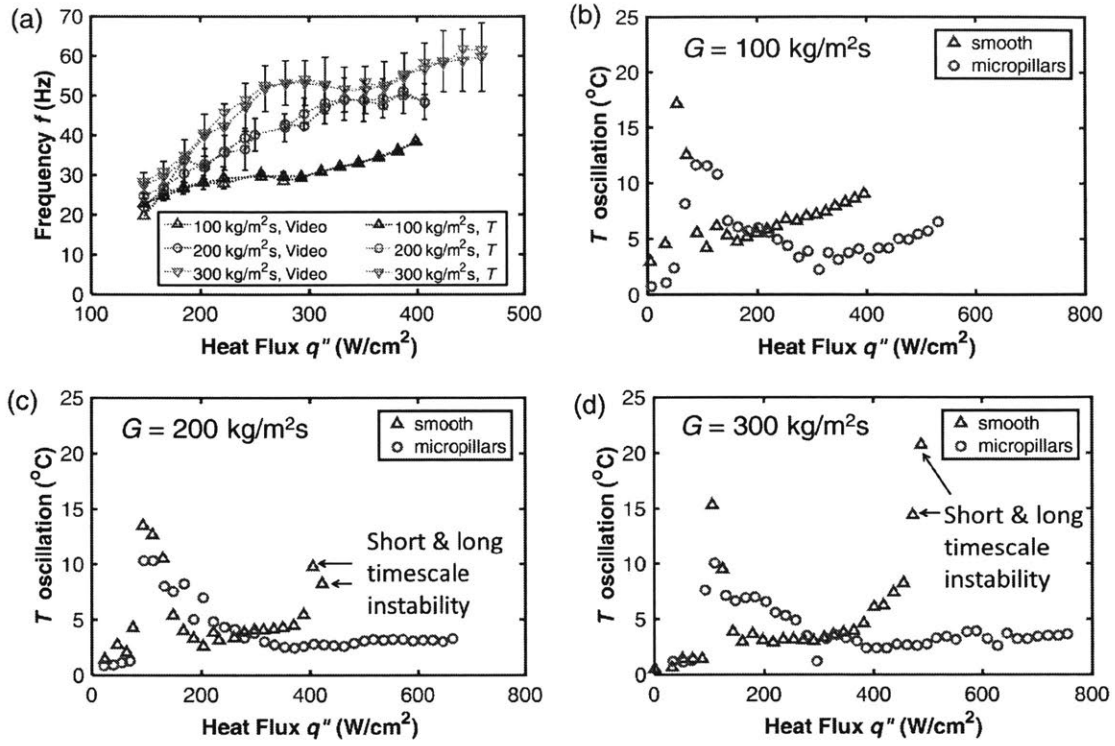

Figure 4-11 The frequency and magnitude of the fast temperature oscillations. (a) The frequency of the temperature oscillations plotted against the heat flux and mass flux for the smooth surface microchannel. The error bars are the standard deviation of a Gaussian fit of the FFT result. The magnitude of the temperature oscillation at a mass flux of (b) 100 kg/m^{2}s, (c) 200 kg/m^{2}s and (d) 300 kg/m^{2}s, respectively, for both the smooth surface and structured surface microchannels. The magnitude was calculated based on 5 to 95 percentile (5% of all the measured temperature is below or above the bounds). The error bars for *T* oscillation is approximately 1 °C.

We further calculated the magnitude of the temperature oscillations (based on 5 and 95 percentile as described previously) as shown in Figure 4-11b-d. The peaks at low heat flux are due to flow instability (wait time approximately 0.1-1 seconds) following the ONB. As the heat flux increases, bubbles are generated more frequently and the temperature (*T*) oscillation reduces. For the smooth surface microchannel, the *T* oscillations increased again at high heat fluxes (annular regime) due to dry-out (as discussed in Figure 4-8), and the gradual increase of the dry-out duration. In comparison, the structured surface delayed and suppressed dry-out due to capillary wicking, and the magnitude of the *T* oscillations remained small. This allowed the structured surface

microchannel to achieve high heat fluxes (700 W/cm^2, Figure 4-11c and d) with stable temperatures.

Figure 4-11b-d also suggests that the short-timescale T oscillations are most severe at a low mass flux (100 kg/m^{2}s). As the mass flux increased to 200 and 300 kg/m^{2}s, the magnitude of the short-timescale T oscillations (without the presence of long-timescale instability) decreased. For example, at the same heat flux of 400 W/cm^2, the T oscillations decreased from 9 °C to 5 °C as the mass flux increased from 100 to 300 kg/m^{2}s. This is because the higher mass flux conditions had higher oscillation frequencies that reduced the duration of complete dry-out in each oscillation cycle.

At very high heat fluxes, we also observed long-timescale flow instability which led to large-magnitude T spikes. This behavior is indicated by the sharp increase of the T oscillation magnitude of the last two data points in Figure 4-11c and d (labeled by the arrows). The long-timescale flow instability is usually associated with premature CHF conditions.[23] Figure 4-12 shows the measured temperature during long-timescale oscillations (q"=495 W/cm^2, G=300 kg/m^{2}s) for the smooth surface microchannel. Within the long-timescale temperature oscillations, short-timescale oscillations coexisted. Possible causes for these modes include density-wave type oscillations (short-timescale) and pressure-drop type oscillations (long-timescale).[12] The additional short-timescale instability during the long-timescale instability can also increase the risk of system failure, which has been previously overlooked. The results in Figure 4-11 indicate that surface structures are effective to suppress both modes of instabilities.

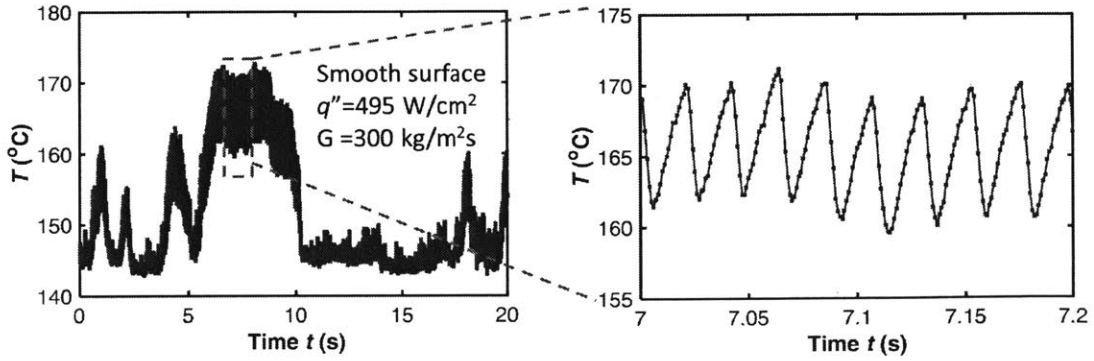

Figure 4-12 Temperature measured by RTD3 for the smooth surface microchannel at q"=495 W/cm^2 and G=300 kg/m^{2}s.

In conclusion, we investigated temperature oscillations as a result of the high-frequency flow oscillation in microchannels and the effect of surface microstructures on the resulting temperature oscillations. Our major observations are as follows.

1. Both short timescale (ms) and long-timescale (s) instabilities can exist in microchannels. The long-timescale instability (usually associated with system compressibility) can cause temperature excursion (~ a few seconds). The short-timescale instability (rapid dry-out and rewetting within the microchannel) can result in fast rate of temperature change with high oscillational frequency and is a reliability concern.
2. Short-timescale flow oscillations can lead to fast and large temperature oscillations due to periodic dry-out and rewetting. The wicking surface structures can suppress dry-out and reduce the temperature oscillations. The structured surfaces are especially beneficial at high heat fluxes and during the annular flow regime. At low heat fluxes where vapor quality is low, T oscillation is mainly due to switching between single-phase and two phase flow. The structured surfaces do not help in this regime where promoting nucleation is the key. An ideal microchannel would promote nucleation at low heat fluxes and promote wetting at high heat fluxes.
3. The frequency of the short-timescale oscillations increases with increasing mass flux. The duration of dry-out in each cycle reduces and the resulting temperature oscillations also reduce. Increasing the mass flux can reduce the magnitude of the short-timescale T oscillations.

Our study suggests that using hydrophilic structures that promote capillary wicking is promising for reducing high-frequency temperature oscillation (thermal fatigue) in high heat flux two-phase microchannel thermal management devices. Future work will include incorporating high-precision pressure sensors locally at the microchannel to investigate the role of surface structures on the pressure drop instability.

Chapter 5

Summary and Future Work

5.1 Summary of Thesis

This thesis focused on investigating the role of surface structures on two-phase microchannel heat sinks. We first aimed to optimize the structures to promote capillary wicking and maximize the dry-out heat flux in a constant vapor pressure environment. Based on the modeling, we integrated surface structures into microchannels to help sustain film evaporation and to suppress dry-out. We investigated the effect of structures on CHF and flow instabilities with timescales from milliseconds to seconds.

The modeling framework we developed can predict the fluid velocity and pressure field in micropillar wick surfaces under any given heat flux, and the maximum heat flux before dry-out occurs. The main challenge of developing such a model is that the liquid-vapor interface varies along the wick surface and is coupled with fluid pressure and velocity. Direct modeling of the entire surface with hundreds and thousands of micropillars is numerically impractical. While previous models have incorporated various assumptions, including the dependence of meniscus shapes on the wicking direction, we chose a finite-volume approach, in which each finite volume is the liquid within four

adjacent pillars and the cell-averaged liquid pressure is used to calculate the meniscus shape for that cell. For typical wicking microstructures that generate much higher capillary pressure than the variation of the liquid pressure within each finite volume, this model can accurately captures the meniscus shape and its variation along the wicking direction. We show the model predictions of the dry-out heat flux for various micropillar structure geometries (height, pitch, and diameter) in the length scale range of 1–100 μm with water as the working fluid, and the optimal geometries to maximize the dry-out heat flux are suggested ($d/h \sim 0.4$–0.6 and $l/d \sim 3$). The model framework can be expanded and applied to other fluids or water at other saturation conditions when relevant thermal and fluid properties are adjusted. The dry-out heat flux $q_{\text{dry-out}}$ is very sensitive to the wicking length L and is governed by $q_{\text{dry-out}} \sim L^{-2}$. This suggests opportunities to enhance $q_{\text{dry-out}}$ by incorporating multiple reservoir channels inside the wicking area to reduce L. This work can be extended to other micropillar geometries such as squares, but the nonuniformity of the contact angle around a pillar can result in a partial receding and partial pinning state, which needs further consideration.

Guided by the model, we designed a two-phase microchannel heat sink incorporated with micropillar arrays as a platform to study the effect of surface structures on flow boiling in microchannels. There are a few challenges associated with this study. First, flow dynamics of two-phase microchannels is highly coupled with other component in the flow loop, which adds additional complexities in interpreting the measured data for flow boiling. For example, a surge tank upstream of the microchannel can introduce pressure drop type of flow oscillations, even at low heat flux. For the same microchannel sample, such flow oscillations may not be present in a loop without an upstream surge tank. It is important to design an experimental loop that avoids severe flow instabilities from interactions between the microchannel and loop components. In addition, flow boiling behavior is also very sensitive to the level of degassing, contamination, and inlet subcooling. For example, liquid with dissolved air may contribute to an early onset of nucleation, which does not represent the case with completely degassed liquid. Contamination of samples changes the wetting characteristics, which plays an important role. Therefore, these parameters need to be carefully controlled for different samples and experimental conditions.

In this study, we designed a microchannel device that decouples thin film evaporation and nucleation by promoting capillary flow on the bottom heated surface while facilitating nucleation from the sidewalls. The experimental result shows that the structures reduced long-timescale (~s) flow boiling instability significantly in the annular flow regime, and achieved very stable surface temperature and channel pressure drop at high heat fluxes close to CHF. The smooth surface showed frequent temperature spikes (~s) and pressure drop fluctuations due to dry-out, which developed gradually to CHF. Visualization of the flow pattern indicates that the micropillar surface can promote capillary flow and increase flow stability by maintaining a stable annular flow and high-performance thin film evaporation. This stabilized annular flow and thin film evaporation contributed to an enhanced HTC and CHF (maximum 57%) compared to a smooth surface microchannel. The pressure drop across all devices was similar, which indicates that the additional pressure drop introduced by the surface structures in this study was negligible. Although this thesis focused on structures that promote capillary wicking, other structures which help entrap vapor to promote and manipulate nucleation of bubbles can also enhance flow boiling, which may be of interest for future study.

The surface structures are also shown to be effective in suppressing the temperature oscillation due to short-timescale flow instabilities. Short-timescale flow oscillations can lead to fast and large temperature oscillations due to periodic dry-out and rewetting. We demonstrated that the wicking surface structures can suppress dry-out and reduce the temperature oscillations. The structured surfaces are especially beneficial at high heat fluxes and during the annular flow regime. At low heat fluxes where vapor quality is low, temperature oscillation is mainly due to switching between single-phase and two phase flow. The structured surfaces do not help in this regime where promoting nucleation is the key. An ideal microchannel would promote nucleation at low heat fluxes and promote wetting at high heat fluxes.

5.2 Future Directions

The studies in this thesis can be extended to a few future directions. First, the study of single length scale structures (micropillars) can be extended to multi length scale structures (microstructures and nanostructures). For single length scale structures,

because capillary driving force and viscous drag are coupled, we need to select the optimal geometry such that the overall dry-out heat flux is maximized. However, in evaporation applications, the heat transfer coefficient is also an important parameter. Enhancing the heat transfer coefficient generally requires small structures with close spacing such that the thin-film area (liquid film thickness ~1 μm) increases. The mismatch between the desired length scales of the structures to achieve high dry-out heat fluxes (>50 μm for large permeability) and high heat transfer coefficients (<1-10 μm for thin-film) leads to compromised performances (Figure 5-1a). Therefore, an interesting future direction is to investigate heat pipe designs with multi-length-scale features to help decouple viscous drag, capillarity and thin-film area (Figure 5-1b). The larger pores or channels (~50-100 μm) provide minimal viscous resistance for efficient fluid transport, the smaller nanostructure coatings or porous membrane (<1-10 μm) provide high capillary pumping limit and minimal thermal resistance. For the design of nanoporous membrane on top of micro supporting structures, both the heat transfer coefficient and dry-out heat flux can potentially be significantly enhanced. For micropillars with nanostructures, the heat transfer coefficient can potentially be increased due to wicking from the liquid between the micropillars on to the nanostructures.

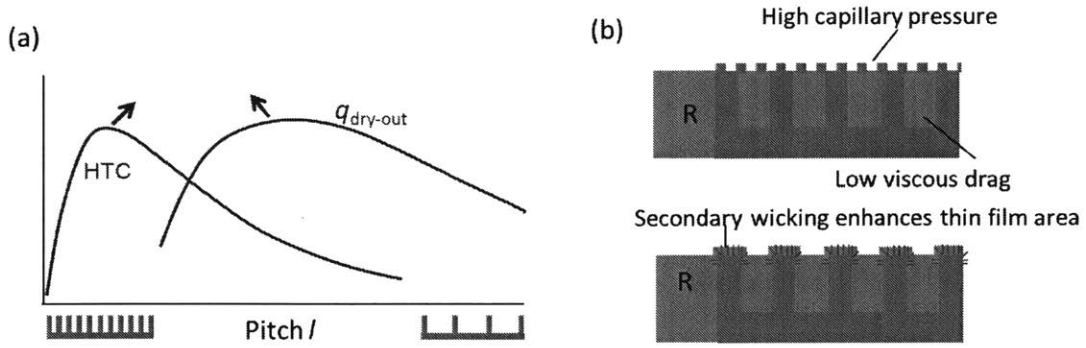

Figure 5-1 (a) Schematic diagram showing the mismatch of the optimal regions for heat transfer coefficient (HTC) and the dry-out heat flux ($q_{dry-out}$) as a function of the pitch of single length scale structures. Arrows indicates the directions for enhancement to reduce the mismatch. (b) Schematic diagrams of multi length scale structures showing nanoporous membranes with micro support structures and micropillars with nanostructure coating.

Another extension towards more fundamental work would be to understand the thermal transport across phase-change interfaces. While significant progress has been

made to promote fluid transport in micro/nanostructures, we still have limited understanding of the thermal transport at the multi-phase interfaces, which is the key to enhancing the heat transfer coefficient. Kinetic theory suggests that heat fluxes during phase change processes may be as high as 10^4 W/cm^2, with heat transfer coefficients of 10^6 W/m^{2}K,[77] but experimentally demonstrated values are orders of magnitude lower than this theoretical prediction due to practical limitations. This suggests that there is much room for improvement. The main challenge has been the difficulty to probe the temperature near the interfaces due to the small length scale. Especially for phase change on micro/nanostructures, it is extremely difficult to fabricate individual temperature sensors onto the micro/nanostructures and to further obtain a temperature mapping. Therefore, new metrological methods, such as a micro-Raman thermography system interfaced with an environmental test stage, can be developed to probe the temperature at the three-phase contact region and to better understand the role of micro/nanostructures in evaporation and condensation processes. Due to their excellent spatial (~1 μm) and temporal (~30 ns) resolution, micro-Raman spectroscopy has been broadly used to study materials properties of semiconductors and optoelectronic devices. There is plenty of opportunity to utilize micro-Raman measurement technique to probe the interfaces to study phase-change heat transfer, which has not been pursued to date.

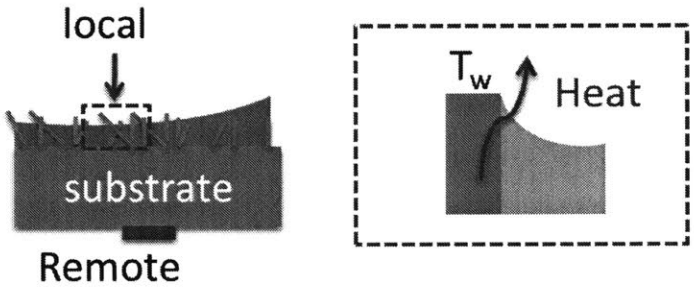

Figure 5-2 Schematic diagram showing current remote temperature measurements and proposed local temperature measurement, with magnified view of heat transport across the interfaces and the local wall temperature.

In the area of flow boiling research, several important future works might include investigating the role of surface structures in parallel multi-channels to scale up the heat sink area and studying the interactions between different channels. Flow boiling of dielectric fluid on structured surfaces is another area of interest because it is more

applicable to electronics cooling. Challenges for dielectric fluids include their low surface tension and latent heat. The design of a high performance two-phase heat sink will likely need to incorporate several enhancement schemes together such as structures that promote capillary wicking, cavities that promote nucleation, and device level design including inlet restrictors and microchannels with expanding cross-sectional area to suppress the reverse flow. The ultimate goal is to develop high-performance and reliable two-phase microchannel heat sink devices that include evaporation/boiling and condensation, which are urgently needed as the power densities continue to increase in electronic systems.

References

(1) Pop, E. Energy Dissipation and Transport in Nanoscale Devices. *Nano Res.* **2010**, *3* (3), 147–169.

(2) Krishnan, S.; Garimella, S. V.; Chrysler, G. M.; Mahajan, R. V. Towards a Thermal Moore's Law. *IEEE Trans. Adv. Packag.* **2007**, *30* (3), 462–474.

(3) *International Technology Roadmap for Semiconductors 2.0, 2015 Edition*; 2015.

(4) Bejan, A. *Advanced Engineering Thermodinamics*; Wiley: New York, 2006.

(5) Pautsch, G. Thermal Challenges in the Next Generation of Supercomputers. *Proceeding Cool. MEECC Conf.* **2005**, 1–83.

(6) Liu, X.; Lienhard, J. H. Extremely High Heat Flux Removal by Subcooled Liquid Jet Impingement. *Fundam. Subcooled Flow Boil. ASME HTD 217*, 11–20.

(7) Mudawar, I. Assessment of High-Heat-Flux Thermal Management Schemes. *IEEE Trans. Compon. Packag. Technol.* **2001**, *24* (2), 122–141.

(8) Deng, W.; Gomez, A. Electrospray Cooling for Microelectronics. *Int. J. Heat Mass Transf.* **2011**, *54* (11–12), 2270–2275.

(9) Wang, E. N.; Zhang, L.; Jiang, L.; Koo, J.-M.; Maveety, J. G.; Sanchez, E. A.; Goodson, K. E.; Kenny, T. W. Micromachined Jets for Liquid Impingement Cooling of VLSI Chips. *J. Microelectromechanical Syst.* **2004**, *13* (5), 833–842.

(10) Zuckerman, N.; Lior, N. Jet Impingement Heat Transfer: Physics, Correlations, and Numerical Modeling. In *Advances in Heat Transfer*; George A. Greene, J. P. H., Avram Bar-Cohen and Young I.Cho, Ed.; Elsevier, 2006; Vol. 39, pp 565–631.

(11) Zuber, N. Hydrodynamic Aspects of Boiling Heat Transfer, California. Univ., Los Angeles; and Ramo-Wooldridge Corp., Los Angeles, 1959.

(12) Kakac, S.; Bon, B. A Review of Two-Phase Flow Dynamic Instabilities in Tube Boiling Systems. *Int. J. Heat Mass Transf.* **2008**, *51* (3–4), 399–433.

(13) Kariya, H. A.; Peters, T. B.; Cleary, M.; Hanks, D. F.; Staats, W. L.; Brisson, J. G.; Wang, E. N. Development and Characterization of an Air-Cooled Loop Heat Pipe With a Wick in the Condenser. *J. Therm. Sci. Eng. Appl.* **2013**, *6* (1), 011010–011010.

(14) Wayner, P. C.; Kao, Y. K.; LaCroix, L. V. The Interline Heat-Transfer Coefficient of an Evaporating Wetting Film. *Int. J. Heat Mass Transf.* **1976**, *19* (5), 487–492.

(15) Cho, H. J.; Preston, D. J.; Zhu, Y.; Wang, E. N. Nanoengineered Materials for Liquid–vapour Phase-Change Heat Transfer. *Nat. Rev. Mater.* **2016**, *2*, 16092.

(16) Palko, J. W.; Zhang, C.; Wilbur, J. D.; Dusseault, T. J.; Asheghi, M.; Goodson, K. E.; Santiago, J. G. Approaching the Limits of Two-Phase Boiling Heat Transfer: High Heat Flux and Low Superheat. *Appl. Phys. Lett.* **2015**, *107* (25), 253903.

(17) Dai, X.; Yang, F.; Yang, R.; Huang, X.; Rigdon, W. A.; Li, X.; Li, C. Biphilic Nanoporous Surfaces Enabled Exceptional Drag Reduction and Capillary Evaporation Enhancement. *Appl. Phys. Lett.* **2014**, *105* (19), 191611.

(18) Adera, S.; Antao, D.; Raj, R.; Wang, E. N. Design of Micropillar Wicks for Thin-Film Evaporation. *Int. J. Heat Mass Transf.* **2016**, *101*, 280–294.
(19) Ćoso, D.; Srinivasan, V.; Lu, M.-C.; Chang, J.-Y.; Majumdar, A. Enhanced Heat Transfer in Biporous Wicks in the Thin Liquid Film Evaporation and Boiling Regimes. *J. Heat Transf.* **2012**, *134* (10), 101501–101501.
(20) Li, D.; Wu, G. S.; Wang, W.; Wang, Y. D.; Liu, D.; Zhang, D. C.; Chen, Y. F.; Peterson, G. P.; Yang, R. Enhancing Flow Boiling Heat Transfer in Microchannels for Thermal Management with Monolithically-Integrated Silicon Nanowires. *Nano Lett.* **2012**, *12* (7), 3385–3390.
(21) Yang, F.; Dai, X.; Peles, Y.; Cheng, P.; Khan, J.; Li, C. Flow Boiling Phenomena in a Single Annular Flow Regime in Microchannels (I): Characterization of Flow Boiling Heat Transfer. *Int. J. Heat Mass Transf.* **2014**, *68*, 703–715.
(22) Yang, F.; Dai, X.; Peles, Y.; Cheng, P.; Khan, J.; Li, C. Flow Boiling Phenomena in a Single Annular Flow Regime in Microchannels (II): Reduced Pressure Drop and Enhanced Critical Heat Flux. *Int. J. Heat Mass Transf.* **2014**, *68*, 716–724.
(23) Zhu, Y.; Antao, D. S.; Chu, K.-H.; Chen, S.; Hendricks, T. J.; Zhang, T.; Wang, E. N. Surface Structure Enhanced Microchannel Flow Boiling. *J. Heat Transf.* **2016**, *138* (9), 91501.
(24) Pop, E. Energy Dissipation and Transport in Nanoscale Devices. *Nano Res.* **2010**, *3* (3), 147–169.
(25) Mahajan, R.; Chiu, C.; Chrysler, G. Cooling a Microprocessor Chip. *Proc. IEEE* **2006**, *94* (8), 1476–1486.
(26) Majumdar, A. Thermoelectric Devices: Helping Chips to Keep Their Cool. *Nat. Nanotechnol.* **2009**, *4* (4), 214–215.
(27) Kandlikar, S. G.; Kuan, W. K.; Willistein, D. A.; Borrelli, J. Stabilization of Flow Boiling in Microchannels Using Pressure Drop Elements and Fabricated Nucleation Sites. *J. Heat Transf.* **2005**, *128* (4), 389–396.
(28) Zhu, Y.; Antao, D. S.; Bian, D. W.; Zhang, T. J.; Wang, E. N. Reducing Instability and Enhancing Critical Heat Flux Using Integrated Micropillars in Two-Phase Microchannel Heat Sinks. In *2015 Transducers - 2015 18th International Conference on Solid-State Sensors, Actuators and Microsystems (TRANSDUCERS)*; 2015; pp 343–346.
(29) Weibel, J. A.; Garimella, S. V.; North, M. T. Characterization of Evaporation and Boiling from Sintered Powder Wicks Fed by Capillary Action. *Int. J. Heat Mass Transf.* **2010**, *53* (19–20), 4204–4215.
(30) Nam, Y.; Sharratt, S.; Byon, C.; Kim, S. J.; Ju, Y. S. Fabrication and Characterization of the Capillary Performance of Superhydrophilic Cu Micropost Arrays. *J. Microelectromechanical Syst.* **2010**, *19* (3), 581–588.
(31) Ranjan, R.; Patel, A.; Garimella, S. V.; Murthy, J. Y. Wicking and Thermal Characteristics of Micropillared Structures for Use in Passive Heat Spreaders. *Int. J. Heat Mass Transf.* **2012**, *55* (4), 586–596.
(32) Hale, R. S.; Ranjan, R.; Hidrovo, C. H. Capillary Flow through Rectangular Micropillar Arrays. *Int. J. Heat Mass Transf.* **2014**, *75*, 710–717.
(33) Xiao, R.; Enright, R.; Wang, E. N. Prediction and Optimization of Liquid Propagation in Micropillar Arrays. *Langmuir* **2010**, *26* (19), 15070–15075.

(34) Wang, Y. X.; Peterson, G. P. Analytical Model for Capillary Evaporation Limitation in Thin Porous Layers. *J. Thermophys. Heat Transf.* **2003**, *17* (2), 145–149.
(35) Ravi, S.; Horner, D.; Moghaddam, S. Monoporous Micropillar Wick Structures, I-Mass Transport Characteristics. *Appl. Therm. Eng.* **2014**, *73* (1), 1371–1377.
(36) Horner, D.; Ravi, S.; Moghaddam, S. Monoporous Micropillar Wick Structures, II-Optimization & Theoretical Limits. *Appl. Therm. Eng.* **2014**, *73* (1), 1378–1386.
(37) Brinkman, H. C. A Calculation of the Viscous Force Exerted by a Flowing Fluid on a Dense Swarm of Particles. *Appl. Sci. Res.* **1949**, *1* (1), 27–34.
(38) Du, S.-Y.; Zhao, Y.-H. Numerical Study of Conjugated Heat Transfer in Evaporating Thin-Films near the Contact Line. *Int. J. Heat Mass Transf.* **2012**, *55* (1–3), 61–68.
(39) Spivak, M. *A Comprehensive Introduction to Differential Geometry*, 3rd Edition.; Publish or Perish, 1999; Vol. 3.
(40) COMSOL Multiphysics. *User Manual, v. 5.0*; 2015.
(41) Kandlikar, S. G. A Theoretical Model to Predict Pool Boiling CHF Incorporating Effects of Contact Angle and Orientation. *J. Heat Transf.* **2001**, *123* (6), 1071–1079.
(42) Chu, K.-H.; Enright, R.; Wang, E. N. Structured Surfaces for Enhanced Pool Boiling Heat Transfer. *Appl. Phys. Lett.* **2012**, *100* (24), 241603.
(43) Raj, R.; Maroo, S. C.; Wang, E. N. Wettability of Graphene. *Nano Lett.* **2013**, *13* (4), 1509–1515.
(44) Weibel, J. A.; Kim, S. S.; Fisher, T. S.; Garimella, S. V. Carbon Nanotube Coatings for Enhanced Capillary-Fed Boiling from Porous Microstructures. *Nanoscale Microscale Thermophys. Eng.* **2012**, *16* (1), 1–17.
(45) Zhang, C.; Hong, F.; Cheng, P. Simulation of Liquid Thin Film Evaporation and Boiling on a Heated Hydrophilic Microstructured Surface by Lattice Boltzmann Method. *Int. J. Heat Mass Transf.* **2015**, *86*, 629–638.
(46) Thome, J. R. The New Frontier in Heat Transfer: Microscale and Nanoscale Technologies. *Heat Transf. Eng.* **2006**, *27* (9), 1–3.
(47) Krishnan, S.; Garimella, S. V.; Chrysler, G. M.; Mahajan, R. V. Towards a Thermal Moore's Law. *IEEE Trans. Adv. Packag.* **2007**, *30* (3), 462–474.
(48) Kandlikar, S. G. Fundamental Issues Related to Flow Boiling in Minichannels and Microchannels. *Exp. Therm. Fluid Sci.* **2002**, *26* (2–4), 389–407.
(49) Das, P. K.; Chakraborty, S.; Bhaduri, S. Critical Heat Flux During Flow Boiling in Mini And Microchannel-A State of The Art Review. *Front. Heat Mass Transf.* **2012**, *3* (1).
(50) Bergles, A. E.; V, J. H. L.; Kendall, G. E.; Griffith, P. Boiling and Evaporation in Small Diameter Channels. *Heat Transf. Eng.* **2003**, *24* (1), 18–40.
(51) Hetsroni, G.; Mosyak, A.; Pogrebnyak, E.; Segal, Z. Explosive Boiling of Water in Parallel Micro-Channels. *Int. J. Multiph. Flow* **2005**, *31* (4), 371–392.
(52) Zhang, T.; Peles, Y.; Wen, J. T.; Tong, T.; Chang, J.-Y.; Prasher, R.; Jensen, M. K. Analysis and Active Control of Pressure-Drop Flow Instabilities in Boiling Microchannel Systems. *Int. J. Heat Mass Transf.* **2010**, *53* (11–12), 2347–2360.

(53) Zhang, T.; Tong, T.; Chang, J.-Y.; Peles, Y.; Prasher, R.; Jensen, M. K.; Wen, J. T.; Phelan, P. Ledinegg Instability in Microchannels. *Int. J. Heat Mass Transf.* **2009**, *52* (25–26), 5661–5674.
(54) Yadigaroglu, G.; Bergles, A. E. Fundamental and Higher-Mode Density-Wave Oscillations in Two-Phase Flow. *J. Heat Transf.* **1972**, *94* (2), 189–195.
(55) Bergles, A. E.; Kandlikar, S. G. On the Nature of Critical Heat Flux in Microchannels. *J. Heat Transf.* **2005**, *127* (1), 101–107.
(56) Koşar, A.; Kuo, C.-J.; Peles, Y. Suppression of Boiling Flow Oscillations in Parallel Microchannels by Inlet Restrictors. *J. Heat Transf.* **2005**, *128* (3), 251–260.
(57) Wang, G.; Cheng, P.; Bergles, A. E. Effects of Inlet/outlet Configurations on Flow Boiling Instability in Parallel Microchannels. *Int. J. Heat Mass Transf.* **2008**, *51* (9–10), 2267–2281.
(58) Koşar, A.; Kuo, C.-J.; Peles, Y. Boiling Heat Transfer in Rectangular Microchannels with Reentrant Cavities. *Int. J. Heat Mass Transf.* **2005**, *48* (23–24), 4867–4886.
(59) David, M. P.; Steinbrenner, J. E.; Miler, J.; Goodson, K. E. Adiabatic and Diabatic Two-Phase Venting Flow in a Microchannel. *Int. J. Multiph. Flow* **2011**, *37* (9), 1135–1146.
(60) Alexander, B. R.; Wang, E. N. Design of a Microbreather for Two-Phase Microchannel Heat Sinks. *Nanoscale Microscale Thermophys. Eng.* **2009**, *13* (3), 151–164.
(61) Fazeli, A.; Mortazavi, M.; Moghaddam, S. Hierarchical Biphilic Micro/nanostructures for a New Generation Phase-Change Heat Sink. *Appl. Therm. Eng.* **2015**, *78*, 380–386.
(62) Koşar, A.; Peles, Y. Boiling Heat Transfer in a Hydrofoil-Based Micro Pin Fin Heat Sink. *Int. J. Heat Mass Transf.* **2007**, *50* (5–6), 1018–1034.
(63) Wang, Y.; Peles, Y. Subcooled Flow Boiling in a Microchannel with a Pin Fin and a Liquid Jet in Crossflow. *Int. J. Heat Mass Transf.* **2015**, *86*, 165–173.
(64) Woodcock, C.; Yu, X.; Plawsky, J.; Peles, Y. Piranha Pin Fin (PPF) — Advanced Flow Boiling Microstructures with Low Surface Tension Dielectric Fluids. *Int. J. Heat Mass Transf.* **2015**, *90*, 591–604.
(65) Dhir, V. K. Boiling Heat Transfer. *Annu. Rev. Fluid Mech.* **1998**, *30* (1), 365–401.
(66) Chen, R.; Lu, M.-C.; Srinivasan, V.; Wang, Z.; Cho, H. H.; Majumdar, A. Nanowires for Enhanced Boiling Heat Transfer. *Nano Lett.* **2009**, *9* (2), 548–553.
(67) Li, C.; Wang, Z.; Wang, P.-I.; Peles, Y.; Koratkar, N.; Peterson, G. P. Nanostructured Copper Interfaces for Enhanced Boiling. *Small* **2008**, *4* (8), 1084–1088.
(68) Ahn, H. S.; Jo, H. J.; Kang, S. H.; Kim, M. H. Effect of Liquid Spreading due to Nano/microstructures on the Critical Heat Flux during Pool Boiling. *Appl. Phys. Lett.* **2011**, *98* (7), 71908.
(69) Rahman, M. M.; Ölçeroğlu, E.; McCarthy, M. Role of Wickability on the Critical Heat Flux of Structured Superhydrophilic Surfaces. *Langmuir* **2014**, *30* (37), 11225–11234.

(70) Chu, K.-H.; Soo Joung, Y.; Enright, R.; Buie, C. R.; Wang, E. N. Hierarchically Structured Surfaces for Boiling Critical Heat Flux Enhancement. *Appl. Phys. Lett.* **2013**, *102* (15), 151602-151602–151604.
(71) Betz, A. R.; Jenkins, J.; Kim, C.-J. "CJ"; Attinger, D. Boiling Heat Transfer on Superhydrophilic, Superhydrophobic, and Superbiphilic Surfaces. *Int. J. Heat Mass Transf.* **2013**, *57* (2), 733–741.
(72) Betz, A. R.; Xu, J.; Qiu, H.; Attinger, D. Do Surfaces with Mixed Hydrophilic and Hydrophobic Areas Enhance Pool Boiling? *Appl. Phys. Lett.* **2010**, *97* (14), 141909.
(73) Shin, S.; Choi, G.; Kim, B. S.; Cho, H. H. Flow Boiling Heat Transfer on Nanowire-Coated Surfaces with Highly Wetting Liquid. *Energy* **2014**, *76*, 428–435.
(74) Kleinstreuer, C.; Koo, J. Computational Analysis of Wall Roughness Effects for Liquid Flow in Micro-Conduits. *J. Fluids Eng.* **2004**, *126* (1), 1–9.
(75) Bahrami, M.; Yovanovich, M. M.; Culham, J. R. Pressure Drop of Fully Developed, Laminar Flow in Rough Microtubes. *J. Fluids Eng.* **2005**, *128* (3), 632–637.
(76) Hsu, Y. Y. On the Size Range of Active Nucleation Cavities on a Heating Surface. *J. Heat Transf.* **1962**, *84* (3), 207–213.
(77) Carey, V. P. *Liquid Vapor Phase Change Phenomena: An Introduction to the Thermophysics of Vaporization and Condensation Processes in Heat Transfer Equipment, Second Edition*; Taylor & Francis, 2007.
(78) Rao, S. R.; Peles, Y. Spatiotemporally Resolved Heat Transfer Measurements for Flow Boiling in Microchannels. *Int. J. Heat Mass Transf.* **2015**, *89*, 482–493.
(79) Rao, S. R.; Houshmand, F.; Peles, Y. Transient Flow Boiling Heat-Transfer Measurements in Microdomains. *Int. J. Heat Mass Transf.* **2014**, *76*, 317–329.
(80) Lemmon, E. W.; Huber, M. L.; McLinden, M. O. *NIST Standard Reference Database 23*; National Institute of Standards and Technology, 2013.
(81) Kuo, C.-J.; Peles, Y. Flow Boiling Instabilities in Microchannels and Means for Mitigation by Reentrant Cavities. *J. Heat Transf.* **2008**, *130* (7), 072402–072402.
(82) Wu, H. Y.; Cheng, P. Visualization and Measurements of Periodic Boiling in Silicon Microchannels. *Int. J. Heat Mass Transf.* **2003**, *46* (14), 2603–2614.
(83) Zhu, Y.; Antao, D. S.; Lu, Z.; Somasundaram, S.; Zhang, T.; Wang, E. N. Prediction and Characterization of Dry-out Heat Flux in Micropillar Wick Structures. *Langmuir* **2016**.
(84) Antao, D. S.; Adera, S.; Zhu, Y.; Farias, E.; Raj, R.; Wang, E. N. Dynamic Evolution of the Evaporating Liquid–Vapor Interface in Micropillar Arrays. *Langmuir* **2016**, *32* (2), 519–526.
(85) Mönig, R.; Keller, R. R.; Volkert, C. A. Thermal Fatigue Testing of Thin Metal Films. *Rev. Sci. Instrum.* **2004**, *75* (11), 4997–5004.
(86) Ledinegg, M. Instability of Flow during Natural and Forced Circulation. *Waerme* **1938**, *61* (8), 891–898.
(87) Stenning, A. H. Instabilities in the Flow of a Boiling Liquid. *J. Basic Eng.* **1964**, *86* (2), 213–217.
(88) Manavela Chiapero, E.; Fernandino, M.; Dorao, C. A. Review on Pressure Drop Oscillations in Boiling Systems. *Nucl. Eng. Des.* **2012**, *250*, 436–447.

(89) Zhang, T. Transient Characteristics and Control of Active Thermal Management Systems. *Annu. Rev. Heat Transf.* **2015**, *18*, 284–285.
(90) Zhu, Y.; Antao, D. S.; Zhang, T.; Wang, E. N. Suppressed Dry-out in Two-Phase Microchannels via Surface Structures. *J. Heat Transf.* **2016**, *138* (8), 080905–080905.
(91) Alam, T.; Khan, A. S.; Li, W.; Yang, F.; Tong, Y.; Khan, J.; Li, C. Transient Force Analysis and Bubble Dynamics during Flow Boiling in Silicon Nanowire Microchannels. *Int. J. Heat Mass Transf.* **2016**, *101*, 937–947.
(92) Bigham, S.; Moghaddam, S. Microscale Study of Mechanisms of Heat Transfer during Flow Boiling in a Microchannel. *Int. J. Heat Mass Transf.* **2015**, *88*, 111–121.
(93) Mita, J.; Qu, W. Pressure Drop of Water Flow across a Micro-Pin–fin Array Part 2: Adiabatic Liquid–vapor Two-Phase Flow. *Int. J. Heat Mass Transf.* **2015**, *89*, 1007–1015.
(94) Deng, D.; Wan, W.; Qin, Y.; Zhang, J.; Chu, X. Flow Boiling Enhancement of Structured Microchannels with Micro Pin Fins. *Int. J. Heat Mass Transf.* **2017**, *105*, 338–349.
(95) Heo, K. Y.; Kihm, K. D.; Lee, J. S. Fabrication and Experiment of Micro-Pin-Finned Microchannels to Study Surface Roughness Effects on Convective Heat Transfer. *J. Micromechanics Microengineering* **2014**, *24* (12), 125025.
(96) Chu, K.-H.; Xiao, R.; Wang, E. N. Uni-Directional Liquid Spreading on Asymmetric Nanostructured Surfaces. *Nat. Mater.* **2010**, *9* (5), 413–417.
(97) Zhu, Y.; Antao, D. S.; Xiao, R.; Wang, E. N. Real-Time Manipulation with Magnetically Tunable Structures. *Adv. Mater.* **2014**, *26* (37), 6442–6446.
(98) Zhu, Y.; Antao, D. S.; Lu, Z.; Somasundaram, S.; Zhang, T.; Wang, E. N. Prediction and Characterization of Dry-out Heat Flux in Micropillar Wick Structures. *Langmuir* **2016**, *32* (7), 1920–1927.
(99) Bian, D. W. Enhanced Flow Boiling Heat Transfer in Microchannels with Structured Surfaces at Varied Mass Flow Rates. Thesis, Massachusetts Institute of Technology, 2015.